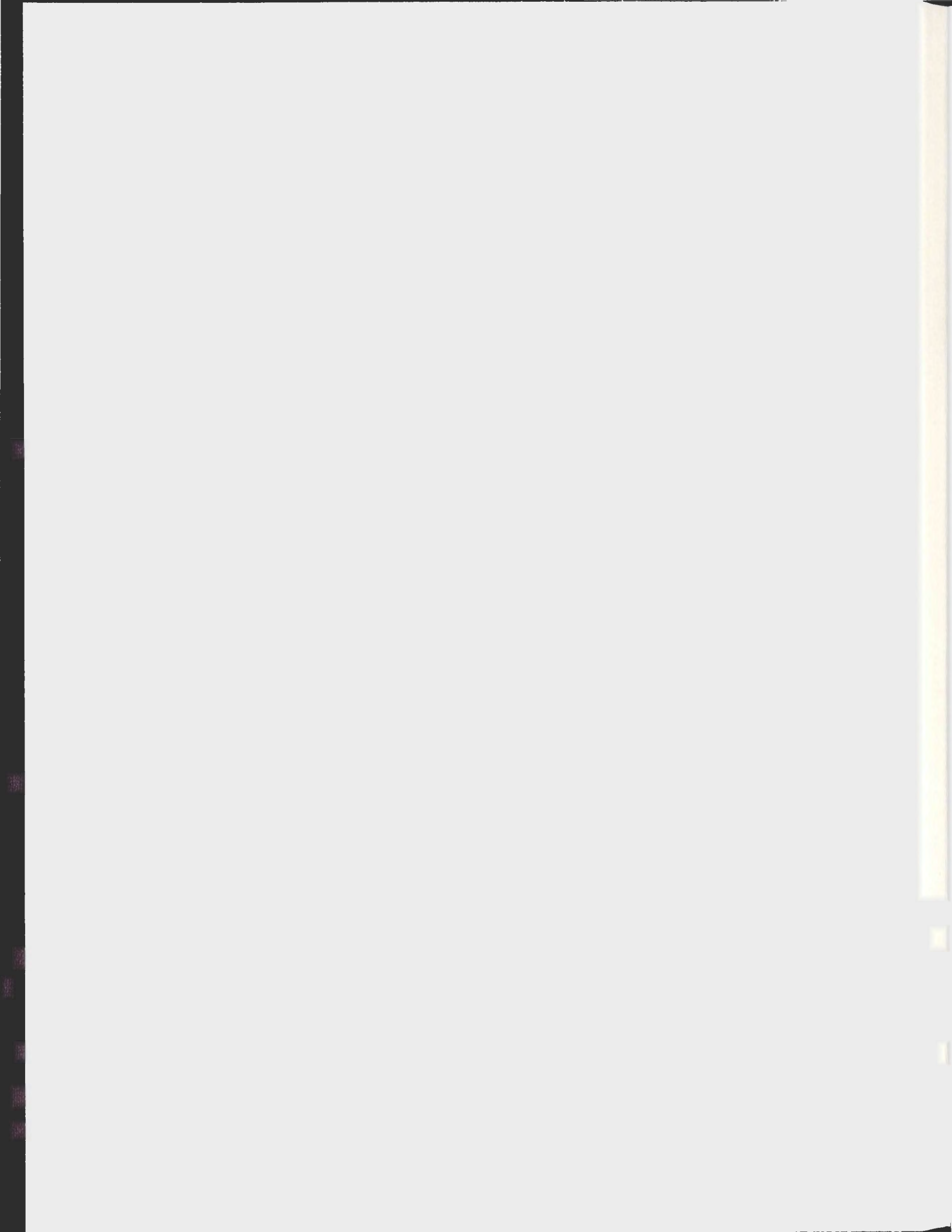


SIMULATION OF TEMPERATURE AND CURRENTS
IN PLACENTIA BAY

ZHIMIN MA



Simulation of Temperature and Currents in Placentia Bay

by

© zhimin ma

A thesis submitted to the School of Graduate Studies in partial fulfillment of
the requirements for the degree of Master of Science
Department of Physics and Physical Oceanography
Memorial University of Newfoundland
August, 2010

St. John's

Newfoundland

Abstract

A three-dimensional circulation model is applied to better understand the circulation and physical processes in Placentia Bay. The model is based on the finite-volume coastal ocean model (FVCOM) with the vertical eddy viscosity calculated from a level 2.5 revised turbulence closure scheme with 21 unequally spaced vertical levels. The model is forced at the lateral open boundaries with 5 tidal constituents and at the surface with wind and heat flux based on meteorological observations at Argentia. The open boundary temperature and salinity and non-tidal sea level are derived from a larger-scale shelf model. Temperature and currents are hindcast for spring 1999. Simulated tidal elevations agree well with tide-gauge data. The Root Mean Square Difference of the model tidal currents was 40% relative to observations. The model temperature and non-tidal currents show reasonable agreement with moored measurements. The model simulates many features of the Bay, including the seasonal evolution of stratification, cyclonic circulation in the out bay and late-spring upwelling on the western side of the outer bay.

Acknowledgment

I would like to thank Prof. Guoqi Han and Prof. Brad de Young for the assistance and guidance during my graduate program.

Thanks to Dr. Brad de Young for providing the observed data for comparison.

Thanks to Dr. Changsheng Chen for providing the model code.

Table of Contents

Abstract	ii
Acknowledgments	iii
List of Tables	vi
List of Figures	viii
Chapter 1 Introduction	1
1.1 Placentia Bay	1
1.2 Oceanographic Observation in Placentia Bay	2
1.3 Modeling in Placentia Bay	3
1.4 Objective	4
1.5 Outline of Thesis	5
Chapter 2 Hydrodynamic Equations	6
2.1 Basic Equation	6
2.2 Vertically Integrated Equation (External mode)	9
2.3 Turbulent Closure Model and Horizontal Mixing Coefficient	11
2.4 Velocity and Temperature Boundary Treatment at the Surface and Bottom	13
2.5 Model Domain and Model Grid	15
2.6 Open Boundary Condition and Treatment	18
2.7 Initial Conditions	22
2.8 Meteorological Forcing	25
2.9 Model Runs and Parameterization	25
Chapter 3 Data	27
3.1 Mooring Data for Comparison	27
3.2 Tide-gauge Observation	33
3.3 Data Analysis Method	34
Chapter 4 Tides and Tidal Currents	37
4.1 Tidal Elevation and Comparison	37
4.2 Tidal Currents and Comparison	40
Chapter 5 Currents, Temperature	46
5.1 Sea-level Comparison at Argentia	46
5.2 Comparison of Observed and Simulated Temperature	48
5.3 Comparison of Observed and Simulated Vertical Temperature	61

5.4 Seasonal Surface Temperature Pattern	63
5.5 Time Series Comparison of Currents	68
5.6 Vertical Currents Profile	74
5.7 Horizontal Mean Circulation	77
5.8 Transport	80
Chapter 6 Summary and Future Work	83
References	86

List of Tables

- Table 3-1. Statistics for the 20m observed currents for M1 to M4. Observed currents are separated into three months. M stands for the mean of the data and V means the variance of the data. 29
- Table 3-2. Statistics for the 55m observed currents for M1 to M3 and 45m observed currents at M4. Observed currents are separated into three months. M stands for the mean of the data and V means the variance of the data. 30
- Table 3-3. Statistics for the observed temperature ($^{\circ}$) for M1 to M4 at different depth of 10m, 20m and 30m. Observed temperatures are separated into three months. M stands for the mean of the data and V means the variance of the data. 31
- Table 3-4. Statistics for the observed temperature ($^{\circ}$) for M1 to M4 at different depth of 40m, 55m and 80m. Observed temperatures are separated into three months. M stands for the mean of the data and V means the variance of the data. 31
- Table 3-5. Statistics for the observed temperature ($^{\circ}$) for M2, M3, M5, M6, and M7 at different depth of 75m, 100m and 200m. Observed temperatures are separated into three months. M stands for the mean of the data and V means the variance of the data. 32
- Table 3-6. Statistics for the observed salinity for M1 to M4 at different depth of 20m and 55m. Observed salinity is separated into three months. M stands for the mean of the data and V means the variance of the data. There is measurement error after days 150 at M2, and we marked the star. 32
- Table 4-1. Summary and statistics for observed and computed semidiurnal and diurnal tidal elevation and pressure gauge. AO is the amplitude of the observed site. PO is the phase of the observed site. AMO is the amplitude difference of observed and model results. PMO is the phase difference of observed and model results. 39
- Table 4-2. Statistics of model computed currents for M_2 compared with the observation data 44

Table 5-1. Statistics for 10m model-observation temperature comparison at M1, M2, M3, and M4	58
Table 5-2. Statistics for 20 m model-observation temperature comparison at M1, M2, M3, M4	59
Table 5-3. Statistics for 30 m model-observation temperature comparison at M1, M2, M3 an M4	59
Table 5-4. RMS temperature difference between the observed and simulated value for six sites at 40 m, 55 m, 75 m, 80 m, and 100 m.	59
Table 5-5. Statistics for along bay and cross bay currents for four points at 20m. VDR and SDR index are calculated for currents.	73
Table 5-6. Statistics for along bay and cross bay currents for four points at 55m. VDR and SDR index are calculated for currents.	74

List of Figures

- Figure 2-1. Map of model domain showing the major locations and features, bathymetry (100m contour, 200m contour). Complicated topography can be seen at the head of the Bay. (The bathymetry data is from ETOP5 before smoothing, and m_map is used to plot this figure) 17
- Figure 2-2. The horizontal finite element grid (named as pb during running) used in the numerical model. 18
- Figure 2-3. Climatological temperature ($^{\circ}\text{C}$) at (a) surface and (b) bottom in spring and at (c) surface and (d) bottom in summer 24
- Figure 3-1. Map showing the locations of coastal tide gauge (NF-8 and NF-9) with crosses, and current meter mooring sites with circle. These circle points have depths of 106m, 182m, 165m, 55m, 428m, 304m and 147m separately. M1 and M2 are located at the west side of the bay, while M3 and M4 are at the east side of bay. M5, M6, and M7 are moored at the head of bay around the three main islands. 33
- Figure 4-1. M_2 and K_1 coamplitude and cophase chart. Amplitude contour line is shown as red color and phase line is in blue color. 100 m and 200 m isobaths are displayed as a thin solid line. 39
- Figure 4-2. M_2 tidal current ellipses (a) near surface and (b) near bottom, and (c) K_1 , (d) O_1 current ellipses near surface. The 100m and 200m isobaths is displayed as a thin solid line. 43
- Figure 4-3. Scatter diagram of the M_2 tidal current amplitude and phase for zonal and meridional velocity. (a) amplitude of U. (b) phase of U. (c) amplitude of V. (d) phase of V. 45
- Figure 5-1. (a) wind forcing in Argentina, (b) inverse barometric effect from st.john's station air pressure data, (c) 36 hour low pass filtered sea level comparison. 47

- Figure 5-2. Time-series temperature comparison of filtered(36-h low-pass filter) observed(red line) and simulated(blue line) for six points at different depths (a)observed and model temperature for M1 and M2 at 10 m.(b) observed and model temperature for M3 and M4 at 20 m .(c) observed and model temperature for M1 at 20 m (d) observed and model temperature for M3 and M4 at 20 m (e) observed and model temperature for M1 and M2 at 30 m (f) observed and model temperature for M3 and M4 at 30 m (g) observed and model temperature for M1 and M2 at 40 m (h) observed and model temperature for M3 and M4 at 40m (i) observed and model temperature for M1 and M2 at 55 m (j) observed and model temperature for M3 at 55 m and M4 at 45 m (k) observed and model temperature for M5 and M6 at 75meter(l) observed and model temperature for M2 and M3 at 80 m (m) observed and model temperature for M2 at 100 m 50
- Figure 5-3. Comparison of the vertical temperature profile between the model results and observation for the six points on (a) April 15, (b) May 1, (c) June 15. 61
- Figure 5-4. Surface circulation and temperature surface field at two different time for (a):April-19-18:00 and (b): June-15-0:00 65
- Figure 5-5. Temperature transect along the 47 degree at two different time point (a):April-19-18:00 and (b) June-15-0:00. 67
- Figure 5-6. Time-series currents comparison of filtered (36-h low-pass filter) observed (red line) and simulated (blue line) for four points at different depths. (a) observed and model along bay and cross bay currents for M1 and M2 at 20 m (b) observed and model along bay and cross bay currents for M3 and M4 at 10 m (c) observed and model along bay and cross bay currents for M1 and M2 at 55 m (d) observed and model along bay and cross bay currents for M4 at 40 m. 71
- Figure 5-7. Velocity transect along the 47 °N at three different time point (a):April-19-18:00 and (b) May-21-0:00 (c) June-15-0:00. 76
- Figure 5-8. Model mean currents from year day 94.75 to 182 at the (a) 20m below the surface and (b) $\sigma = 0.9975$ circulation. 79
- Figure 5-9. Map showing the Placentia Bay. The isobaths displayed are 100 and 200m. Avalon channel(AC) (a) transect locationThree transport times series plots for (b) Avalon Channel (between 100m contour) (c) transect at 47 °N . Values are detided using the 36 cutoff frequency low filter. 81

List of Symbols

σ	sigma coordinate from 0 to -1
ξ	free surface elevation(m)
D	water depth plus sea level(m)
H	bottom depth(m)
K_m	vertical turbulent viscosity(m^2/s)
K_h	vertical diffusivity (m^2/s)
ρ	potential density(kg/m^3)
A_m	horizontal viscosity(m^2/s)
A_h	horizontal diffusivity(m^2/s)
T	potential temperature($^{\circ}$)
S	salinity(psu)
q^2	twice the turbulent kinetic energy (m^2/s^2)
l	turbulent length scale
u	eastward velocity(m/s)
v	northward velocity(m/s)
ω	sigma coordinate vertical velocity(m/s)
κ	von Karman constant=0.4

1 Introduction

1.1 Placentia Bay

Placentia Bay is located at the southern part of the Newfoundland Island and is bordered by Burin Peninsula to the west and the Avalon Peninsula to the east. The mean circulation is driven by the westward current from the inshore branch of the Labrador Current that flows into the bay on the eastern side, continues along the coastline and flows outside the bay on the western side (Hart *et al.*, 1999; Schillinger *et al.*, 2000; Bradbury *et al.*, 2000). There are important fisheries in the Bay which have received considerable interest recently because of potential ecological sensitivity and economic impacts (Bradbury *et al.*, 2000). For example, Rose *et al.* (2000) found that Atlantic cod off the eastern coast of Newfoundland had undergone a rapid decrease in abundance and recognized the importance of localized coastal populations (Ruzzante *et al.*, 2000; Snelgrove *et al.*, 2008). In coastal areas such as Placentia Bay, currents may be less influenced by the cold Labrador Current and more by local processes, such as wind forcing (deYoung *et al.* 1993) which can contribute to the transport and changes in larval fish abundance (Pepin *et al.*, 1995). For Atlantic cod, *Gadus morhua*, evidence is increasing that spawning occurs in multiple coastal areas of

Newfoundland (Smedbol *et al.* 1998; Lawson and Rose 2000). Compared with offshore habitats, coastal spawning may lead to increased survival due to decreased predation and higher growth rates resulting from higher prey densities (Frank and Leggett, 1982; Taggart and Leggett, 1987; Pepin *et al.* 1995). As a result, following the right site hypothesis proposed by deYoung and Rose (1993) for Atlantic cod, Placentia Bay is one of the few areas in Atlantic Canada where spawner biomass and, therefore, egg and larval supplies are reasonably healthy. Bradbury *et al.* (2000) and Bradbury *et al.* (2008) found that spawning was concentrated in three areas: Perch Rock (eastern outer bay), Bar Haven (inner bay), and Oderin Bank (western outer bay). They also observed that the peak in late-stage eggs occurred on the western side of the bay. The upwelling along the head and western side of the bay during summer may cause enhanced primary and secondary production. There is also heavy ship traffic on the eastern side of Placentia Bay since many industrial and business activities occur there. As a result, there is an increasing need to understand physical dynamic processes in Placentia Bay.

1.2 Oceanographic Observation in Placentia Bay

In last two decades many *in situ* observations have been made in the

Placentia Bay region. Hart *et al.* (1999) and Scillinger *et al.* (2000) deployed four and seven moorings during two separate years in Placentia Bay to detect the mean circulation pattern and seasonal current variability. Temperature and salinity observations were also made to better understand the hydrography in Placentia Bay.

Recently, extensive efforts have been made to understand the physical, chemical and biological processes of Placentia Bay such as the Smart Bay Project launched by the Marine Institute of Memorial University in early 2000s (<http://www.smartbay.ca/>). The Smart Bay Project regularly collects oceanographic data at fixed stations along the western and eastern side of Placentia Bay.

1.3 Modeling in Placentia Bay

Quantitative knowledge and dynamical understanding of the three-dimensional shelf circulation has expanded for the Newfoundland and Labrador shelf and slope region including Placentia Bay. Petrie and Anderson (1983) estimated the mean circulation and transport based on various data sources. Greenberg and Petrie (1998) presented the barotropic mean circulation in the Grand Banks region of continental shelf off eastern Canada using a barotropic numerical model, showing notable discrepancies

between observed and modeled flows. Tang *et al.*, (1996) studied several aspects of the circulation and volume transport using a linear three-dimensional diagnostic model. Han (2005) investigated the barotropic wind-driven circulation over the Newfoundland and Labrador shelf using a three-dimensional finite element model. Han *et al.* (2008) examined the seasonal variability of the Labrador Current and shelf circulation off Newfoundland using a semi-prognostic model. These shelf models had insufficient resolution for Placentia Bay, and thus offer little insight into circulation in the Bay. Therefore, a high resolution numerical model focused on the Placentia Bay region is warranted to hindcast, nowcast and forecast circulation variability and to complement observations of the Smart Bay Project.

1.4 Objective

The objective of this study is to develop a three-dimensional (3D) high resolution ocean model for the Placentia Bay region to accurately simulate tidal currents and the wind- and density-driven circulation. This is a local-area simulation for Placentia Bay and the solution will be compared with hydrographic data from Hart *et al.* (1999). This is the first application of

a high resolution state-of-the-art 3D prognostic primitive equation ocean model in Placentia Bay.

1.5 Outline of Thesis

Section 2 describes the basic equations of the circulation model and boundary conditions including initial condition with hydrography data used for initial condition in input files, such as temperature and salinity, open boundary conditions and surface external forcing boundary conditions. The model domain and grid layout are presented in section 2. The data used for comparison are presented in section 3, and the mooring data are compared with the model results. Model results and the analysis method are also detailed in this section. In section 4, the observed and modeled tidal currents in Placentia Bay are presented and compared. Section 5 details the prognostic running to acquire the currents and temperature. The comparisons and statistics are also discussed. Section 6 provides a discussion and summary.

2 Hydrodynamic Equations

2.1 Basic Equation

The numerical model used for this study is an unstructured grid, finite-volume, three-dimensional, primitive equation, finite-volume coastal ocean model (FVCOM; Chen *et al.*, 2003). In general, two numerical methods are used in the ocean modelling. One is the finite-difference method (Blumberg and Mellor 1987; Blumberg 1994), the other is finite-element method (Lynch and Naimie 1993; Naimie 1996). The finite difference approach is computationally more efficient, but is less capable of resolving the complicated coastal boundary. Using the triangular mesh, the finite element method can more easily and most accurately fit the irregular coastal. This method, however, had difficulty to conserve mass and momentum. The finite volume method integrates the momentum and tracers through individual unit control volume and solved numerically by flux through the volume boundaries to guarantee the conservation of mass and momentum.

FVCOM is a sigma coordinate, free surface, hydrostatic model. It uses time splitting method for computational efficiency including the internal mode and external mode. Both modes are constrained by its Courant-Friedriches-Levy (CFL) condition. A second order accuracy, fourth order

Runge-Kutta time stepping scheme is used for the external time integration, while a first order Euler time stepping scheme is selected for the internal time integration. A second order accurate upwind scheme, which is based piecewise for linear reconstruction of dynamic variable, is used for the spatial flux calculation for momentum and tracer values (Kobayashi *et al.*, 1999; Hubbard, 1999). Furthermore, Huang *et al.* (2008) have examined the hydraulic jump case and found a method, known as the multidimensional slope limiting method (Barth and Jespersen, 1989; Hubbard, 1999), had the advantage of reproducing the discontinuities without introducing oscillations associated with the finite volume scheme. For a more accurate estimation of sea level, currents, and the salt and temperature flux, velocity variables are placed at centroids, while all scalar variables are placed at nodes.

The basic equations are presented in a bottom following, sigma coordinate system in order to obtain a smooth representation of irregular variable bottom topography. The σ coordinate transformation is defined as

$$\sigma = \frac{z - \xi}{H + \zeta} = \frac{z - \xi}{D}$$

where σ varies from -1 at the bottom to 0 at the surface, z is the z coordinate, ξ is the free sea level, H is the bottom depth and D is the water depth. Under this coordinate system, the momentum and continuity equations are given as (2-1) - (2-3), where u, v, w are the eastward, northward

and upward velocity, K_m and ρ are the turbulent viscosity and potential density; and thermodynamic equations are as (2-4)-(2-6), where T and S are the temperature and salinity, K_h is the vertical diffusivity and \hat{H} is the heat source term.

$$\frac{\partial \xi}{\partial t} + \frac{\partial Du}{\partial x} + \frac{\partial Dv}{\partial y} + \frac{\partial \omega}{\partial \sigma} = 0 \quad (2-1)$$

$$\frac{\partial uD}{\partial t} + \frac{\partial u^2 D}{\partial x} + \frac{\partial uvD}{\partial y} + \frac{\partial u\omega}{\partial \sigma} - fvD \quad (2-2)$$

$$= -gD \frac{\partial \xi}{\partial x} - \frac{gD}{\rho_0} \left[\frac{\partial}{\partial x} (D \int_{\sigma}^0 \rho d\sigma') + \sigma \rho \frac{\partial D}{\partial x} \right] + \frac{1}{D} \frac{\partial}{\partial \sigma} (K_m \frac{\partial u}{\partial \sigma}) + DF_x$$

$$\frac{\partial vD}{\partial t} + \frac{\partial v^2 D}{\partial y} + \frac{\partial uvD}{\partial x} + \frac{\partial v\omega}{\partial \sigma} + fuD \quad (2-3)$$

$$= -gD \frac{\partial \xi}{\partial x} - \frac{gD}{\rho_0} \left[\frac{\partial}{\partial y} (D \int_{\sigma}^0 \rho d\sigma') + \sigma \rho \frac{\partial D}{\partial y} \right] + \frac{1}{D} \frac{\partial}{\partial \sigma} (K_m \frac{\partial v}{\partial \sigma}) + DF_y$$

$$\frac{\partial TD}{\partial t} + \frac{\partial TuD}{\partial x} + \frac{\partial TvD}{\partial y} + \frac{\partial T\omega}{\partial \sigma} = \frac{1}{D} \frac{\partial}{\partial \sigma} (K_h \frac{\partial T}{\partial \sigma}) + D\hat{H} + DF_T \quad (2-4)$$

$$\frac{\partial SD}{\partial t} + \frac{\partial SuD}{\partial x} + \frac{\partial SvD}{\partial y} + \frac{\partial S\omega}{\partial \sigma} = \frac{1}{D} \frac{\partial}{\partial \sigma} (K_h \frac{\partial S}{\partial \sigma}) + DF_S \quad (2-5)$$

$$\rho = \rho(T, S) \quad (2-6)$$

In the σ coordinate system, the horizontal diffusion terms are defined as:

$$DF_x \approx \frac{\partial}{\partial x} [2A_m H \frac{\partial u}{\partial x}] + \frac{\partial}{\partial y} [A_m H (\frac{\partial u}{\partial y} + \frac{\partial v}{\partial x})] \quad (2-7)$$

$$DF_y \approx \frac{\partial}{\partial y} [2A_m H \frac{\partial v}{\partial y}] + \frac{\partial}{\partial x} [A_m H (\frac{\partial u}{\partial y} + \frac{\partial v}{\partial x})] \quad (2-8)$$

$$D(F_T, F_S, F_{q^2}, F_{q^2l}) \approx \left[\frac{\partial}{\partial x} (A_h H \frac{\partial}{\partial x}) + \frac{\partial}{\partial y} (A_h H \frac{\partial}{\partial y}) \right] (T, S, q^2, q^2l) \quad (2-9)$$

where A_m and A_h are the horizontal eddy and thermal diffusion coefficients,

respectively.

2.2 Vertically Integrated Equation (External mode)

The vertically integrated equation (2-10 to 2-12) illustrates the external mode based on the mode splitting method (Madala and Piacsek, 1977). The external mode is for the fast moving motion, while the internal mode is responsible for the slow moving motion. Since a fast moving gravity wave exists in ocean, sea level should be computed for the external mode. Because sea level is proportional to the gradient of the water transport, it can be computed using the vertically integrated equations. Then the 3D internal model equations can be solved for a given sea level.

$$\frac{\partial \xi}{\partial t} + \frac{\partial(\bar{u}D)}{\partial x} + \frac{\partial(\bar{v}D)}{\partial y} = 0, \quad (2-10)$$

$$\begin{aligned} \frac{\partial \bar{u}D}{\partial t} + \frac{\partial(\bar{u}^2 D)}{\partial x} + \frac{\partial(\bar{u}\bar{v}D)}{\partial y} - f\bar{v}D = -gD \frac{\partial \xi}{\partial x} - \frac{gD}{\rho_0} \left\{ \int_{-1}^0 \frac{\partial}{\partial x} (D \int_{\sigma}^0 \rho d\sigma') d\sigma + \frac{\partial D}{\partial x} \int_{-1}^0 \sigma \rho d\sigma \right\} \\ + \frac{\tau_{sx} - \tau_{bx}}{\rho_0} + D\tilde{F}_x + G_x, \end{aligned} \quad (2-11)$$

$$\begin{aligned} \frac{\partial \bar{v}D}{\partial t} + \frac{\partial(\bar{v}^2 D)}{\partial y} + \frac{\partial(\bar{u}vD)}{\partial x} + f\bar{u}D = -gD \frac{\partial \xi}{\partial y} - \frac{gD}{\rho_0} \left\{ \int_{-1}^0 \frac{\partial}{\partial y} (D \int_{\sigma}^0 \rho d\sigma) d\sigma + \frac{\partial D}{\partial y} \int_{-1}^0 \sigma \rho d\sigma \right\} \\ + \frac{\tau_{xy} - \tau_{by}}{\rho_0} + D\tilde{F}_y + G_y, \end{aligned} \quad (2-12)$$

where G_x and G_y are defined as

$$G_x = \frac{\partial \bar{u}^2 D}{\partial x} + \frac{\partial \bar{u}vD}{\partial y} - D\tilde{F}_x - \left[\frac{\partial \bar{u}^2 D}{\partial x} + \frac{\partial \bar{u}vD}{\partial y} - D\bar{F}_x \right] \quad (2-13)$$

$$G_y = \frac{\partial \bar{v}^2 D}{\partial y} + \frac{\partial \bar{u}vD}{\partial x} - D\tilde{F}_y - \left[\frac{\partial \bar{v}^2 D}{\partial y} + \frac{\partial \bar{u}vD}{\partial x} - D\bar{F}_y \right] \quad (2-14)$$

and the horizontal diffusion terms are approximately given by

$$D\tilde{F}_x \approx \frac{\partial}{\partial x} [2\bar{A}_m H \frac{\partial \bar{u}}{\partial x}] + \frac{\partial}{\partial y} [\bar{A}_m H (\frac{\partial \bar{u}}{\partial y} + \frac{\partial \bar{v}}{\partial x})] \quad (2-15)$$

$$D\tilde{F}_y \approx \frac{\partial}{\partial y} [2\bar{A}_m H \frac{\partial \bar{v}}{\partial y}] + \frac{\partial}{\partial x} [\bar{A}_m H (\frac{\partial \bar{u}}{\partial y} + \frac{\partial \bar{v}}{\partial x})] \quad (2-16)$$

$$D\bar{F}_x \approx \frac{\partial}{\partial x} \overline{2A_m H \frac{\partial u}{\partial x}} + \frac{\partial}{\partial y} \overline{A_m H (\frac{\partial u}{\partial y} + \frac{\partial v}{\partial x})}, \quad (2-17)$$

$$D\bar{F}_y \approx \frac{\partial}{\partial y} \overline{2A_m H \frac{\partial v}{\partial y}} + \frac{\partial}{\partial x} \overline{A_m H (\frac{\partial u}{\partial y} + \frac{\partial v}{\partial x})}, \quad (2-18)$$

The overbar “-” denote the vertical integration. \bar{u} and \bar{v} are vertical averaged eastward and northward velocity. τ_{xx} and τ_{bx} are the surface and bottom stress.

Equation (2-10), (2-11), and (2-12) are the continuity and momentum equations expressed in the sigma coordinate system. The right hand side of the momentum equations contains the barotropic, baroclinic, wind stress, horizontal diffusion and dispersion terms separately.

2.3 Turbulent Closure Model and Horizontal Mixing Coefficient

K_m and K_h used in FVCOM are parameterized using the Mellor and Yamada (1982) level 2.5 turbulent closure scheme as modified by Galperin *et al* (1988) for flow-dependent vertical mixing coefficients. Furthermore, wave breaking process defined as some processes to cause large amounts of wave energy to be transformed in turbulent kinetic energy when the amplitude of a breaking wave reaches a critical level, performs well in ocean surface temperature and surface boundary deepening (Stacey 1999; Burchard 2001; Mellor and Blumberg, 2004). This wave physics processing was introduced into the modeling of surface boundary layer and the wave physical parameters were calculated through experiments and process of observation data (Terray *et al.*, 1996, 1997, 2000). The basic equations are shown in (2-19) and (2-20).

$$\frac{\partial q^2}{\partial t} + u \frac{\partial q^2}{\partial x} + v \frac{\partial q^2}{\partial y} + w \frac{\partial q^2}{\partial z} = 2(P_s + P_b - \varepsilon) + \frac{\partial}{\partial z} (K_q \frac{\partial q^2}{\partial z}) + F_q \quad (2-19)$$

$$\frac{\partial q^2 l}{\partial t} + u \frac{\partial q^2 l}{\partial x} + v \frac{\partial q^2 l}{\partial y} + w \frac{\partial q^2 l}{\partial z} = l E_1 (P_s + P_b - \frac{\tilde{W}}{E_1} \varepsilon) + \frac{\partial}{\partial z} (K_q \frac{\partial q^2 l}{\partial z}) + F_l \quad (2-20)$$

where q^2 is the turbulent kinetic energy and l is the turbulent macroscale.

K_q is the vertically eddy diffusion coefficient of the turbulent kinetic energy,

while F_q and F_l demonstrate the horizontal diffusion of the turbulent kinetic

energy and macroscale. P_s and P_b term on the right hand side of these two

equations represent the shear and buoyancy production of turbulent kinetic

energy. $\varepsilon = q^3 / B_1 l$ is the turbulent kinetic energy dissipation rate, and

$W = 1 + E_2 l^2 / (\kappa L)^2$ is a wall proximity function where $L^{-1} = (\xi - z)^{-1} + (H + z)^{-1}$;

$\kappa = 0.4$ is the von Karman constant.

The turbulent kinetic energy and macroscale equations are closed by

defining $K_m = l q S_m$, $K_h = l q S_h$, $K_q = 0.2 l q$ and $1e^{-4}$ is used as the background

vertical eddy viscosity. S_m and S_h are defined as the stability functions

$$\text{where } S_m = \frac{0.4275 - 3.354 G_h}{(1 - 34.676 G_h)(1 - 6.127 G_h)}, \quad S_h = \frac{0.494}{1 - 34.676 G_h} \text{ and } G_h = \frac{l^2 g}{q^2 \rho_0} \rho_z. \quad S_m$$

and S_h are functions of gradient Richardson number and depend on G_h

which has an upper limit of 0.023 for the case of unstable stratification and a

lower bound of -0.28 for the case of stable stratification.

Parameters A_1, A_2, B_1, B_2 and C_1 are given as 0.92, 16.6, 0.74, 10.1 and 0.08

respectively.

The horizontal mixing coefficient in FVCOM can be selected as a constant value or following the Smagorinsky eddy parameterization method (Smagorinsky, 1963). The diffusion coefficient of momentum and tracer value can be expressed by (2-21) using the Smagorinsky horizontal diffusion scheme.

$$A_m = 0.5C\Omega\sqrt{\left(\frac{\partial u}{\partial x}\right)^2 + 0.5\left(\frac{\partial v}{\partial x} + \frac{\partial u}{\partial y}\right)^2 + \left(\frac{\partial v}{\partial y}\right)^2} \quad (2-21)$$

where C is a constant parameter from 0.1 to 0.2 and Ω is the area of the individual momentum control volume or the tracer control volume.

2.4 Velocity and Temperature Boundary Treatment at the Surface and Bottom

a) surface and bottom currents boundary condition are as follows.

$$\begin{aligned} \left(\frac{\partial u}{\partial \sigma}, \frac{\partial v}{\partial \sigma}\right) &= \frac{D}{\rho_0 K_m} (\tau_{sx}, \tau_{sy}) && \text{at the surface} \\ \left(\frac{\partial u}{\partial \sigma}, \frac{\partial v}{\partial \sigma}\right) &= \frac{D}{\rho_0 K_m} (\tau_{bx}, \tau_{by}) && \text{at the bottom} \end{aligned}$$

where τ_{sx} , τ_{sy} , $\tau_{bx} = C_d \sqrt{u^2 + v^2} u$, and $\tau_{by} = C_d \sqrt{u^2 + v^2} v$ are the x and y components of surface wind and bottom stresses. $D = H + \xi$. The drag coefficient C_d in FVCOM is determined by matching a logarithmic layer to

the model at a height z_{ab} above the bottom. $C_d = \max\left[\frac{\kappa^2}{\ln\left(\frac{z_{ab}}{z_o}\right)}, 0.0025\right]$, where

$\kappa = 0.4$ is von Karman's constant and z_0 is the bottom roughness parameter (Chen *et al.*, 2004b).

A zero normal velocity was specified at the land boundary.

b) Surface and bottom condition for temperature

The surface and bottom boundary conditions for temperature are

$$\begin{aligned} \frac{\partial T}{\partial \sigma} &= \frac{D}{\rho c_p K_h} [Q_n(x, y, t) - SW(x, y, \xi, t)], \text{ at } z = \xi(x, y, t) & (2-22) \\ \frac{\partial T}{\partial \sigma} &= \frac{A_H D \tan \alpha}{K_h - A_H \tan^2 \alpha} \frac{\partial T}{\partial n}, \text{ at } z = -H(x, y) \end{aligned}$$

where $Q_n(x, y, t)$ is the surface net heat flux and $SW(x, y, \xi, t)$ is the short wave flux incident at the sea surface. α is the slope of the bottom bathymetry, and n is the horizontal coordinate (Pedlosky 1974; Chen *et al.*, 2004b).

Knowledge of the distribution of solar radiation in the upper ocean is important for modeling physical processes. To simulate the heat flux penetration process, Kraus (1972) first suggested an absorption profile for short wave radiation as a close simulation. This penetration procedure of the shortwave radiation can be expressed as an exponential equation involving two attenuation lengths. However, this assumption yields a poor approximation in the upper ocean. Based on the observations, downward

radiation effects upon the upper ocean in conjunction with wind stress conditions have been improved by (Paulson and Simpson, 1977; Simpson 1981, a, b). Based on their conclusion, Chen *et al.*, 2003b suggested that this approach leads to a more accurate prediction of near surface temperature. The shortwave profile scheme used in the present study is given by (2-23).

$$\hat{H}(x, y, z, t) = \frac{\partial SW(x, y, z, t)}{\rho c_p} \left(\frac{R}{a} e^{z/a} + \frac{1-R}{b} e^{z/b} \right) \quad (2-23)$$

where SW is the shortwave radiation, R is the ratio of the red component of the electromagnetic radiation in the total shortwave radiation and a and b are attenuation lengths for longer and short (blue-green) wavelength components of the shortwave irradiation.

2.5 Model Domain and Model Grid

The model domain is from 53 °W to 56 °W and 45.5 °N to 47.8 °N. (Figure 2-1). The geometry of the domain features some coastal ocean banks. Starting from the east side of the domain, the Avalon Channel is relatively long and straight, extending into the eastern open boundary, connecting the Haddock Channel out of the south boundary. There, this channel joins Green Bank and Whale Bank which is a part of the Grand Banks. On the west side of the domain, lies part of the St. Pierre Bank, which forms two channels

with Green Bank and Burin Peninsula. The shoreline of the bay has many inlets, and is surrounded by fairly steep cliffs. Three small islands, located in upper Placentia Bay, are also a significant feature with the largest being Merasheen and the other two being Red and Long Islands. The center of the mouth of the bay is 200 m deep, while much of the remainder of the bay is roughly 100 m deep. The average depth is around 125 m. There are several areas with deep channels that run along the longitudinal axis of the bay. The east side of the bay has a regular, straight coastal line; while the western side of the bay has many islands and irregular, complicate coastal line.

The governing equations of the model are solved over an unstructured triangular grid whose spacing is largest (3-5 km) along the open boundary and smallest (200 m) along the coastline (Figure 2-2). There are 21 unequally spaced levels in the vertical, with a minimum spacing of around 0.5 m near sea surface and seabed in order to resolve the shear current and thermodynamic process near surface and bottom. The distribution of sigma levels is 0,-0.005, -0.02,-0.045,-0.08,-0.125, -0.18,-0.245, -0.32, -0.405, -0.5, -0.595, -0.68, -0.755, -0.82, -0.875, -0.92,-0.955,-0.98,-0.995,-1.

The bottom topography was mainly derived from the multibeam

bathymetry of the Canadian Hydrographic Service. To minimize the pressure gradient errors (Mellor *et al.*, 1993), the bathymetry has been smoothed. The maximum ocean depth is 351 m and the minimum depth is 5 m. Smoothing can reduce or remove the pressure gradient errors along the places where depth change rapidly, but at the same time, some small topographic features are removed or reduced.

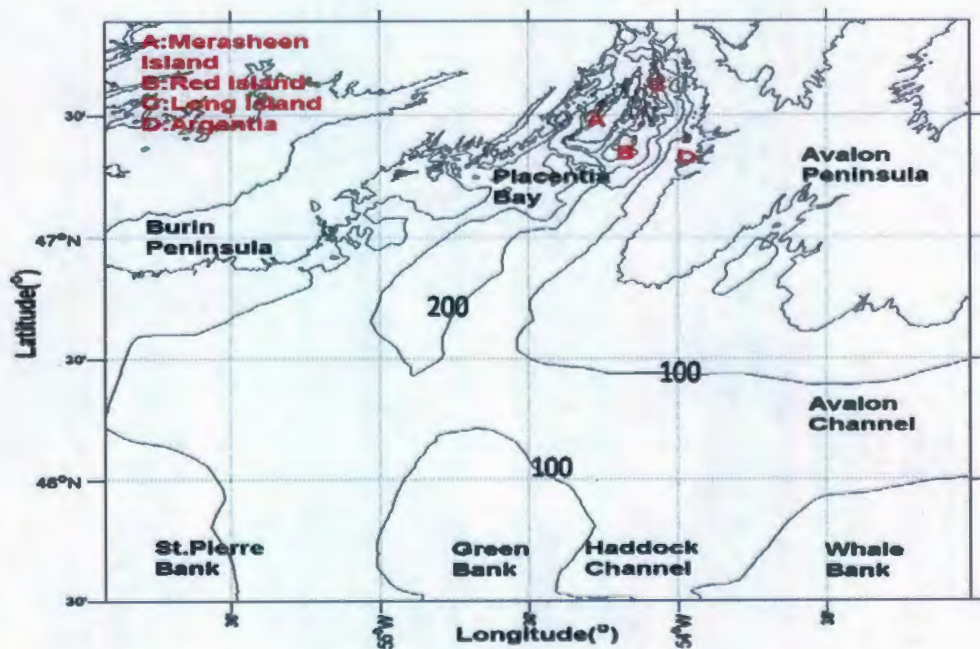
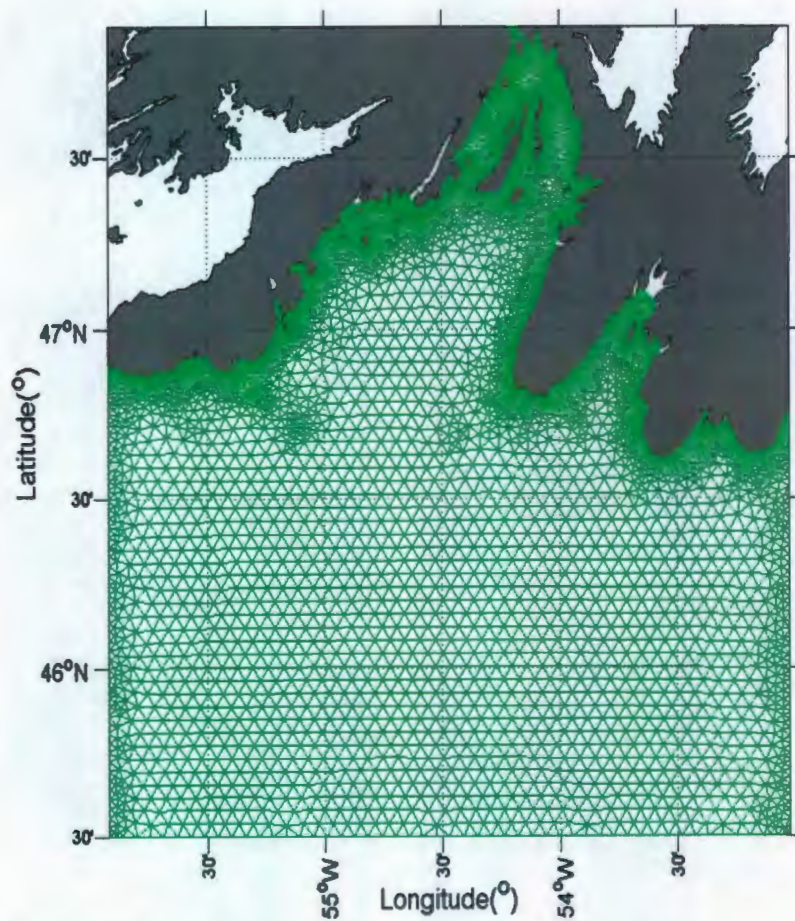


Figure (2-1): Map of model domain showing the major locations and features, bathymetry (100m contour, 200m contour). Complicated topography can be seen at the head of the Bay. (The bathymetry data is from ETOP5 before smoothing, and m_map is used to plot this figure)



Figure(2-2): The horizontal finite element grid(named as pb during running) used in the numerical model.

2.6 Open Boundary Condition and Treatment

1) Open boundary conditions are inevitably involved in regional numerical models. The ideal open boundary schemes are transparent to fluid motion, such as sea level or velocity, which is generated within the model

domain and propagate to the open boundary. Unfortunately, it is not really possible to implement an ideal open boundary scheme. Consequently, the fluid motion is only partially transparent on the open boundary. Chapman (1985) examined seven different radiation open boundary schemes using a barotropic coastal ocean model with a straight coastline and uniform cross-shelf bottom slope. He pointed out that the effect of different open boundary conditions can be determined by different bottom friction as well as the grid size and time step. However, with the inclusion of a varying density effect, open boundary conditions need to be considered with the temperature and salinity flux. Here, a sponge layer is used for velocity and sea-level is fixed at the open boundary. The treatment for temperature and salinity depends on the boundary flux direction.

2) Sea-level at Open Boundary

The open boundary elevation can be obtained through two ways. The first method, which is more accurate, is from tide-gauge data. The second method is from a coarse large model, essentially a nesting method. The second one is not accurate enough, but is widely used and easy to implement. In the current domain, sea level including the 5 tidal constituents (M_2, S_2, N_2, K_1 & O_1) at the open boundary is interpolated from model results

of the Newfoundland shelf simulated with FVCOM. To better estimate the seasonal transport and tidal propagation into the Placentia Bay domain, the Newfoundland Shelf mesh domain was forced with six hourly calculated surface heat flux, observed wind stress and monthly mean elevation at the open boundary from March to June, and then hourly sea level from April 1st to June 30th for the open boundary in Placentia Bay.

3) Velocity on the Open Boundary

The current version of FVCOM provides the sponge-layer method as a boundary condition treatment for velocity. This approach has a user-defined value to be set up before each running, and this coefficient attempts to trap the noise produced by numerical integration at each external time step. However, an excessive or deficient fraction can lead to over-damping or overflow into domain, then result in a velocity discontinuity along the open boundary after long time integrations. As also noted, the boundary velocity can be generated from the boundary sea level gradient. In the current FVCOM model, the sponge layer scheme can be explained based on a nudging scheme. The following equation is the nudging scheme.

$$X^a = \gamma(\bar{X} - X^n) + X^n, \quad (2-24)$$

where X^a is the analysis variable after the nudging at the n th time step, \bar{X} is

the value used for nudging, X^n is the model value at the n th time step, and γ is the nudging coefficient between 0 and 1. Here, if we treat \bar{X} to be 0, then the equation becomes $X^a = X^n - \gamma X^n$ used in the current FVCOM (X is the external velocity) and the model value, X^a , will have a trend to become 0 through model running time. γ is the product of the user defined value and relates to the ratio of the distance from the inner node to the boundary node over user defined radius centered in the boundary node. We can explicitly see if we set γ to be 1, the currents and sea level information can be damped to 0 at the open boundary. To let the 5 tidal constituents (M_2, S_2, N_2, K_1 & O_1) information prorogate in, we then treat γ as a damping time scale around the minimum tidal period(S_2) for the 5 tidal constituents.

4) Temperature and Salinity at Open Boundary

The temperature and salinity open boundary conditions are from the same source as the sea level and velocity at open boundary. Results from a large scale model for the Newfoundland shelf are interpolated to provide the temperature and salinity boundary condition to better avoid underestimating the seasonal change in temperature. In FVCOM, temperature and salinity value at boundary are defined on the node of triangular cells and the volume flux is defined by a net flux through the sections linked to centroids and the

mid-point of the adjacent sides in the surrounding triangles. If the volume flux at the open boundary is propagating out, then the temperature and salinity would be calculated by applying a second-order upwind differential scheme; otherwise, the value is based on the previous time step. Although it is considered a reasonable treatment for temperature and salinity at open boundary, it can also lead to a temperature and salinity jump caused by changing wind. Therefore, we used the Flux Corrected Transport (FCT) scheme which defined as a conservative shock-capturing scheme to efficiently capture this jump.

2.7 Initial Conditions

A) Hydrography Data

The initial temperature and salinity condition have been taken from the monthly-mean temperature and salinity data (Geshelin *et al.*,1999). The temperature and salinity data are provided at standard z-level depths (0,-10,-20,-30, -50, -75, -100,-125,-150,-200,-250,-300, -400, -500, -600, -700, -800,-900,-1000, -1100, -1200, -1300, -1400, -1500, -1750, -2000, -2500, -3000, -3500, -4000, -4500). Then the temperature and salinity data can be interpolated into sigma coordinates. The surface (bottom) temperature fields for spring and summer time are shown in Figure 2-3.

Figure 2-3 shows the initial temperature pattern for spring and summer time. In spring, around $0.6\text{ }^{\circ}\text{C}$ contrasts can be found between the east and west side of the domain. The inshore branch of the Labrador Current carries fresher and colder water into the east side of domain producing temperature fronts as low as $0\text{ }^{\circ}\text{C}$ shown in Figure 2-3(a). This front faces toward the channel between St. Pierre Bank and Green Bank (Figure 2-1). Warmer water can be seen in the 200 m deep basin, extending into the head of the bay, as displayed in the spring bottom temperature plot (Figure 2-3(b)). This plot also shows a significant feature that the weak inshore Labrador Current flows southward along the Avalon Channel, then entering the Haddock Channel. In summer, temperature increases to the south to $13\text{ }^{\circ}\text{C}$ from the head of the bay to the outer open boundary. This regular temperature distribution suggests that the summer temperature in Placentia Bay is strongly influenced by short wave radiation in summer time compared with the dominant source from the Labrador Current in spring time (Figure 2-3(c)). The bottom temperature in summer presents similar thermal feature as in spring with a higher temperature area in the 200 m deep basin (Figure 2-3(d)).

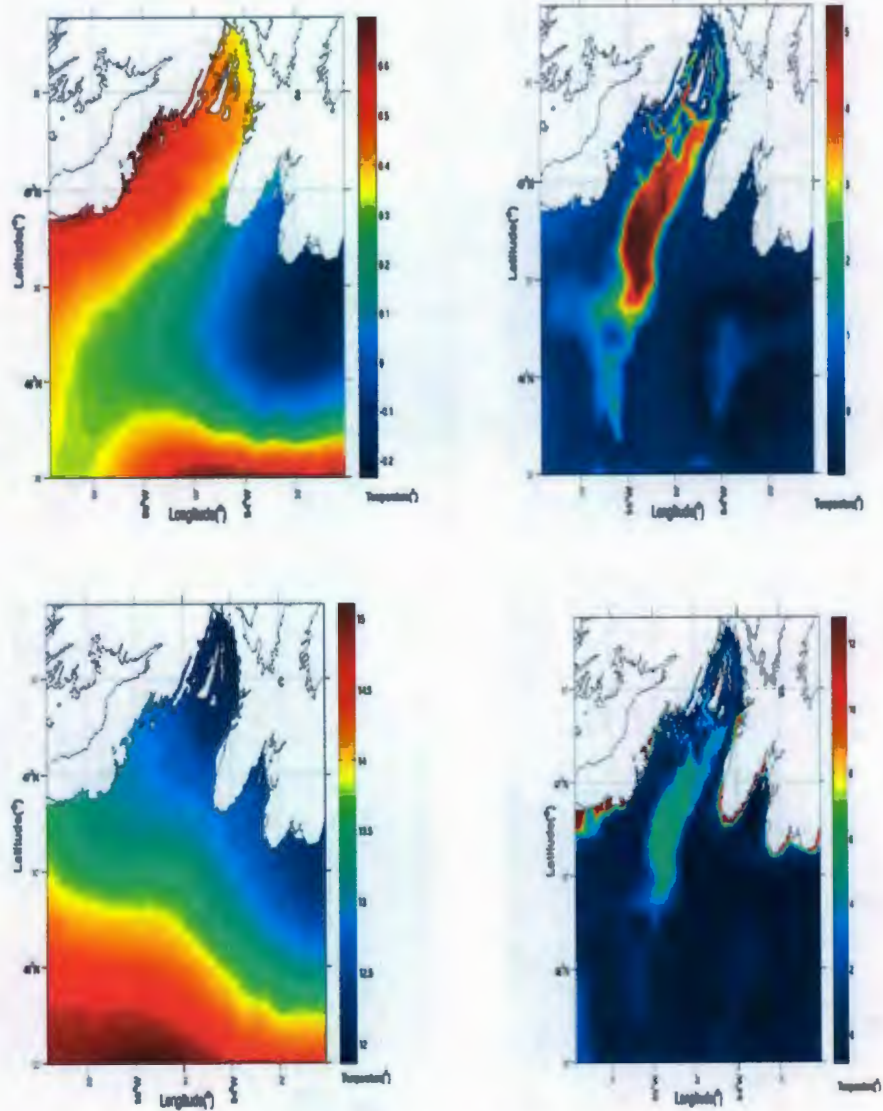


Figure 2-3: Climatological temperature ($^{\circ}C$) at (a) surface and (b) bottom in spring and at (c) surface and (d) bottom in summer.

B) Initial Elevation and Velocity

The initial values of elevation and velocity are specified based on model results of the Newfoundland shelf.

2.8 Meteorological Forcing

Spatially uniform wind stress is used over the whole computational domain. Hourly wind speed and direction and air pressure data collected at Argentinia are applied from April 1 to June 31, 1999. The air pressure data are used to calculate the inverse barometric effect to adjust the observed sea level for comparison with calculated sea level. Heat flux data are calculated from the air-sea toolbox including different functions to calculate shortwave radiation, longwave radiations, latent heat and sensible heat. Surface short wave heat flux was calculated using the relationships of Curry and Webster (1999). A revised function of Li *et al.*, (2006) was used to calculate the albedo including the white cap effect (Monahan and MacNiocaill, 1986) while the modified TOGA COARE code (Fairall *et al.*, 1996) was used to calculate the sensible and latent heat fluxes. The formulation of Fung *et al.*, (1984) was used to estimate longwave radiation based on the sea surface temperature, air temperature, dew temperature, wind speed and cloud cover. Net heat flux and short wave radiation were mapped to the triangular nodes.

2.9 Model Runs and Parameterization

Restricted by the CFL condition, the external time step is 1 second and the internal time step is 10 seconds. The model was run for the period

from April 1 to July 1. The period from April 20 to June 18 is the model analysis interval.

3. Data

3.1 Mooring Data for Comparison

The mooring velocity, salinity and temperature data were taken from the report of Hart *et al.* (1999) which comprised seven current meter moorings deployed around the Bay from the spring to summer of 1999. The locations of the mooring are shown in (Figure 3-1). InterOcean S4's were set at 20 m depth at moorings M1, M2, M3, and M4, while Anderaa RCM7 current meters were moored at 45 (for M4) or 55m at these same points. Acoustic Doppler Current Profiles (ADCPs) were used at moorings M5, M6, and M7 to measure the current velocities. Of these, two were deployed in upward looking mode (M5 and M6) at depth of 110m, while the third was deployed in downward looking mode (M7) at depth of 100m. Unfortunately, we did not obtain the current data in M5, M6 and M7.

The data are recorded in 20 minutes interval and last from year day 108 to 170. The mean and variance value for the 36-hour cutoff filtered data were calculated for each month in Table 3-1 to Table 3-6. M stands for the mean of the value and V stands for the variance; u and v have been converted to the along bay velocity and cross bay velocity defined here. We determined the along-channel and cross-channel axes through a covariance

analysis, which maximized the variance along one component of a set of perpendicular axes. To rotate the co-ordinate system of the axes determined by the covariance analysis required a counter clockwise rotation of around 45° to the Earth axes coordinates at M1 and M2 and around 83° at M3 and M4. For consistency, a counter clockwise rotation of 45° to the Earth Coordinate was used. This rotation was set so that the positive x-axis was approximately parallel to the axis of the Bay. Mean currents at 20m and 55m (Table 3-1 and Table 3-2) show that the along bay velocity is greater than the cross-bay velocity and that the along-bay currents feature more variability based on the variance comparison. These two tables also demonstrate that the velocity decreases with depth; such velocity shear is expected. Seasonal change can be clearly seen with the decreasing strength in currents through April to June. As noted, currents are negative at M1 and M2 while in M3 and M4, the currents are positive. The currents at M3 and M4 on the east side are much stronger than at M1 and M2 on the west side.

We also have temperature data at different depths (Table 3-3 to Table 3-5). Temperature increases with time and reaches a maximum at the end of June. Considering the available vertical temperature profile, the mixed layer could extend deeper to around 50m; and with the increased

surface temperature, the mixed layer depth shallows to around 20m in summer time. Salinity data are available from April to June at 20m and 55m. Shown in the table (Table 3-6), the salinity data at 55m all stay around 32psu and show little variability. However, at 20m, the salinity time series are more interesting with a significantly lower salinity at M2, perhaps caused by the river discharge or measurement error. An unusual high salinity value occurs in M4, with 34psu. We checked the observed salinity value in Station 27 around St.john's, and found the 32 psu salinity value. Therefore, the high salinity value is probably an instrumental error. Thus, we will not make detailed comparisons with the salinity data.

Table 3-1

Statistics for the 20m observed currents for M1 to M4. Observed currents are separated into three months. M stands for the mean of the data and V means the standard deviation of the data.

	April				May			
	U(m/s)		V(m/s)		U(m/s)		V(m/s)	
	M	V	M	V	M	V	M	V
M1	-0.1	0.07	0.03	0.04	-0.06	0.05	0.004	0.03
M2	-0.1	0.05	8e-4	0.04	-0.1	0.06	-0.01	0.03
M3	0.2	0.1	0.1	0.09	0.1	0.07	0.1	0.03
M4	0.1	0.08	0.06	0.02	0.1	0.1	0.04	0.03

June				
	U(m/s)		V(m/s)	
	M	V	M	V
M1	-0.07	0.05	0.004	0.03
M2	-0.1	0.04	5e-4	0.03
M3	0.1	0.05	0.08	0.03
M4	0.1	0.09	0.04	0.03

Table (3-2)

Statistics for the 55m observed currents for M1 to M3 and 45m observed currents at M4. Observed currents are separated into three months. M stands for the mean of the data and V means the variance of the data.

	April				May			
	U(m/s)		V(m/s)		U(m/s)		V(m/s)	
	M	V	M	V	M	V	M	V
M1	-0.07	0.03	-0.002	0.02	-0.04	0.04	3e-4	0.01
M2	-0.08	0.05	-0.007	0.03	-0.07	0.06	-0.02	0.04
M3	X	X	X	X	X	X	X	X
M4	0.07	0.05	0.03	0.04	0.03	0.06	0.01	0.02

June				
	U(m/s)		V(m/s)	
	M	V	M	V
M1	-0.04	0.04	-0.004	0.009
M2	-0.07	0.06	-0.02	0.04
M3	X	X	X	X
M4	0.03	0.05	0.01	0.02

Table 3-3

Statistics for the observed temperature($^{\circ}$) for M1 to M4 at different depth of 10m, 20m and 30m. Observed temperatures are separated into three months. M stands for the mean of the data and V means the variance of the data.

	10 m						20 m					
	Apr		May		June		Apr		May		June	
	M	V	M	V	M	V	M	V	M	V	M	V
M1	1.9	0.2	3.6	1.3	7.6	1.2	1.9	0.2	3.1	1.1	6.8	1.1
M2	1.9	0.2	3.9	1.4	8.5	1.3	X	X	X	X	X	X
M3	1.8	0.2	4.1	1.6	8.8	1.3	1.6	0.2	3.5	1.5	8.0	1.5
M4	1.8	0.4	3.9	1.3	7.7	1.5	1.8	0.3	3.7	1.2	6.3	1.5

	30 m					
	Apr		May		June	
	M	V	M	V	M	V
M1	1.6	0.2	2.2	0.6	4.5	0.9
M2	1.4	0.2	2.4	0.8	4.4	0.8
M3	1.5	0.2	2.2	0.8	3.7	1.3
M4	1.6	0.3	3.0	0.9	3.8	1.4

Table 3-4

Statistics for the observed temperature($^{\circ}$) for M1 to M4 at different depth of 40m, 55m and 80m. Observed temperatures are separated into three months. M stands for the mean of the data and V means the variance of the data.

	40 m						55 m(45 m M4)					
	Apr		May		June		Apr		May		June	
	M	V	M	V	M	V	M	V	M	V	M	V
M1	1.3	0.2	1.8	0.3	2.5	0.4	1.0	0.3	1.3	0.2	1.3	0.2
M2	1.2	0.2	1.8	0.3	2.5	0.5	1.1	0.3	1.4	0.2	1.3	0.4
M3	1.3	0.2	1.5	0.3	1.8	0.5	1.0	0.3	1.1	0.3	1.0	0.4
M4	1.5	0.3	2.2	0.7	2.5	1.0	1.4	0.3	2.0	0.7	2.1	0.8

	80 m(51 m M4)					
	Apr		May		June	
	M	V	M	V	M	V

M1	0.7	0.1	0.8	0.2	0.5	0.2
M2	0.8	0.2	0.9	0.2	0.5	0.2
M3	0.5	0.3	0.3	0.3	0.2	0.3
M4	1.3	0.3	1.6	0.6	1.6	0.6

Table 3-5

Statistics for the observed temperature(°) for M2, M3, M5, M6, and M7 at different depth of 75m, 100m and 200m. Observed temperatures are separated into three months. M stands for the mean of the data and V means the variance of the data.

	75 m(55 m M7)						100 m					
	Apr		May		June		Apr		May		June	
	M	V	M	V	M	V	M	V	M	V	M	V
M5	1.0	0.3	0.9	0.2	0.8	0.3	X	X	X	X	X	X
M6	1.1	0.1	1.0	0.2	1.0	0.3	X	X	X	X	X	X
M7	0.3	0.1	0.6	0.2	0.5	0.3	X	X	X	X	X	X
M2	X	X	X	X	X	X	0.6	0.1	0.6	0.2	0.3	0.1
M3	X	X	X	X	X	X	0.4	0.3	0.07	0.3	-0.1	0.2

	200 m					
	Apr		May		June	
	M	V	M	V	M	V
M5	-0.04	0.06	0.01	0.1	-0.2	0.04
M6	0.1	0.1	-0.1	0.2	-0.3	0.1
M7	X	X	X	X	X	X
M2	X	X	X	X	X	X
M3	X	X	X	X	X	X

Table 3-6

Statistics for the observed salinity for M1 to M4 at different depth of 20m and 55m. Observed salinity is separated into three months. M stands for the mean of the data and V means the variance of the data. There is measurement error after days 150 at M2, and we marked the star.

	20 m					
	Apr		May		June	
	M	V	M	V	M	V
M1	32.6	0.08	32.5	0.1	32.1	0.1
M2	31.6	0.07	31.5	0.1	28.0	3.1*
M3	32.7	0.1	32.3	0.1	31.8	0.1
M4	34.0	0.2	33.9	0.1	33.5	0.2

	55 m					
	Apr		May		June	
	M	V	M	V	M	V
M1	32.3	0.04	32.3	0.03	32.4	0.03
M2	32.3	0.02	32.2	0.02	32.3	0.04
M3	32.4	0.04	32.4	0.06	32.4	0.05
M4	32.3	0.1	32.3	0.08	32.3	0.07

3.2. Tide-gauge Observation

The tidal elevation observation dataset comprised a total of 2 locations. One is located in Argentina and the other is at the very head of bay (Figure 3-1).

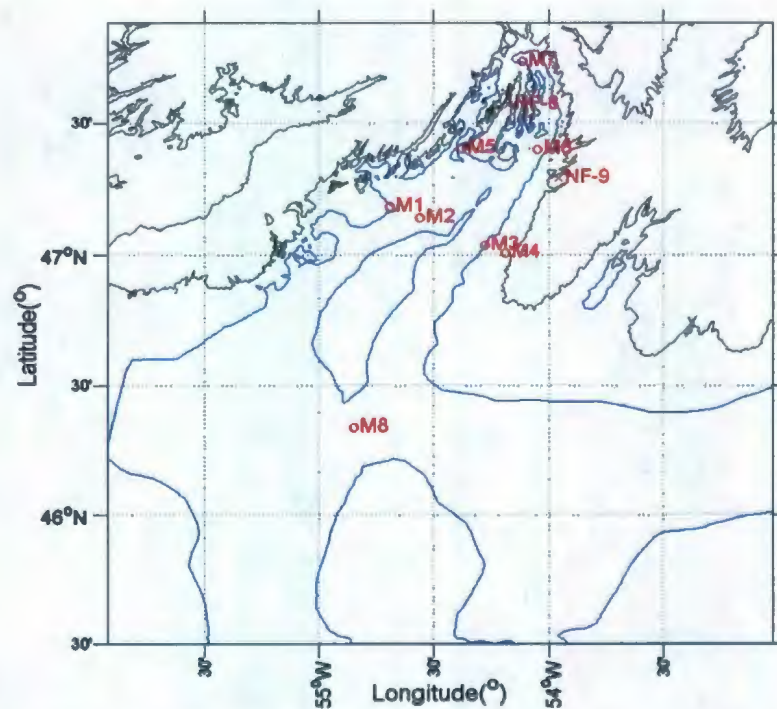


Figure (3-1): Map showing the locations of coastal tide gauge (NF-8, NF-9) with crosses, and current meter mooring sites with circle. These circle points have depths of 106m, 182m, 165m, 55m, 428m, 304m and 147m separately. M1 and M2 are located at the west side of the bay, while M3 and M4 are at the east side of bay. M5, M6, and M7 are moored at the head of bay around the three main islands.

3.3 Data Analysis Method

To evaluate the model solutions quantitatively, moored measurement data were used to compare with the model results.

Temperature and salinity observation data were first filtered using an 8th order low pass Butterworth filter with a cutoff period of 36 hours. Seasonal temperature and salinity variability were better shown after removing the daily change. Considering the dominant five tidal constituents (M_2, S_2, N_2, K_1 & O_1), current mooring and pressure gauge data were filtered using an 8th low pass Butterworth filter with a cutoff frequency corresponding to a period of 36 hours. Data for tidal analysis were first filtered using an 8th order low pass Butterworth filter with a cutoff frequency corresponding to a period of 3 hours. After filtering, the data were sub-sampled to 1 hour intervals and analyzed with t-tide software (Pawlowicz, R *et al.*, 2002).

Six primary goodness-of-fit indices were used here for the residual and tidal current. One is a velocity difference ratio (VDR) defined as the ratio of the sum of the squared magnitudes of the vector velocity differences to the sum of the squared magnitudes of the observed velocities, that is,

$$VDR = \sum |V_m - V_o|^2 / \sum |V_o|^2 \quad (3-1)$$

where V_m is the horizontal model velocity and V_o is the horizontal observational velocity. Lower VDR means better agreement.

The second measure is a speed difference ratio (SDR) defined as the ratio of sum of the Squared speed differences to the sum of the squared magnitudes of the observed velocities, that is,

$$SDR = \frac{\sum (|V_m| - |V_o|)^2}{\sum |V_o|^2} \quad (3-2)$$

The third measure is the root mean square error (RMS):

$$RMS_{error} = \sqrt{\frac{\sum (V_m - V_o)^2}{numel(V_m)}} \quad (3-3)$$

where $numel(V_m)$ is the total number of the compared points.

The fourth measure is the average of the absolute RMS error (abs_RMS), and the relative RMS error (rel_RMS) which are computed for semi-diurnal and diurnal constituents at each observation location of the observed value.

$$abs_RMS = L^{-1} \sum_L D; \quad rel_RMS = L^{-1} \sum_L D / AMP_o \quad (3-4)$$

where D is the RMS difference over a tidal cycle between model and observations, AMP_o is the amplitude of observation and AMP_m is the amplitude of model.

$$D = \left[\frac{1}{2} (AMP_o^2 + AMP_m^2) - AMP_o AMP_m \cos(\phi_o - \phi_m) \right]^{\frac{1}{2}} \quad (3-5)$$

We also used γ^2 to demonstrate the model's ability to simulate the variability of elevations and temperature which is defined as the ratio of the hindcast error variance to the observed variance:

$$\gamma^2 = \frac{Var(O - M)}{Var(O)} \quad (3-6)$$

where Var demotes the variance, and O and M represent observations and model calculated value respectively. A small γ^2 indicates better agreement between the observed and simulated values. If the difference between model results and observation results in a value of Var (O-M) that is greater than Var (O), the γ^2 value can be greater unity. We also note that γ^2 does not take into account the model's bias and could be small if the observed variance is strong.

The final measure is the correlation coefficient between the model and observed data.

4 Tides and Tidal Currents

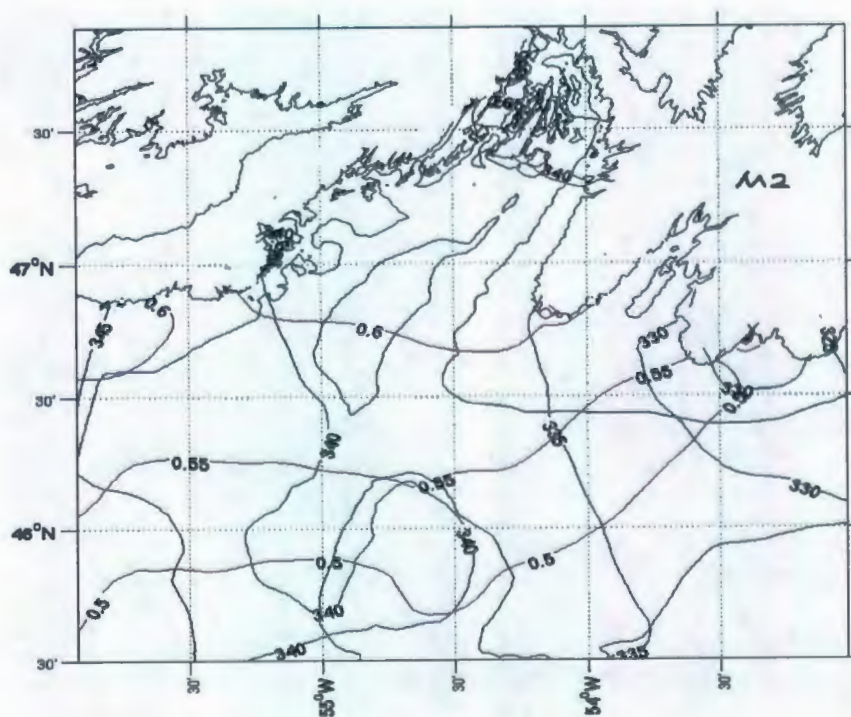
In this chapter we examine the tidal elevation and currents for the five primary tidal constituents (M_2, S_2, N_2, K_1 & O_1), which are obtained using harmonic analysis of the model output from April 20 to June 18, 1999.

4.1 Tidal elevation and Comparison

Figure 4-1 shows the coamplitude and cophase charts of the computed M_2 and K_1 tidal constituents. The M_2 tide propagates from the Avalon channel westward through the model domain and northward toward the head of the bay, with a maximum amplitude of 70 cm. The S_2 and N_2 constituents (not shown) have similar spatial patterns but with amplitude smaller by four to five times, which is consistent with other studies of the semidiurnal tidal constituents in Newfoundland shelf and coastal line (Han, 2000). The diurnal constituent K_1 exhibits a significantly different spatial feature as the semidiurnal constituent. The coamplitude of K_1 increases from east to the west, consistent with an amphidromic point in the Laurentian Channel (Han *et al.*, 1996) west of the model domain. Statistics between computed tidal elevations and observations at coastal tidal gauge are given in Table 4-1. For these two coastal sites, the amplitude difference are below 5 cm, and the phase difference is below 7 degree except for K_1 . The small root mean

square (RMS) differences, 3 cm in amplitude and 4 degree in phase respectively except for K_1 , indicate good agreement of the model result with the observation data, . Other indicators are the absolute RMS_{error} and relative RMS_{error} which account for the both amplitude and phase discrepancies. Compared with the diurnal constituents, the semidiurnal constituents have smaller absolute RMS_{error} and relative RMS_{error} values and therefore show better agreement with observations.

(a) M_2 coamplitude and cophase



(b) K_1 coamplitude and cophase

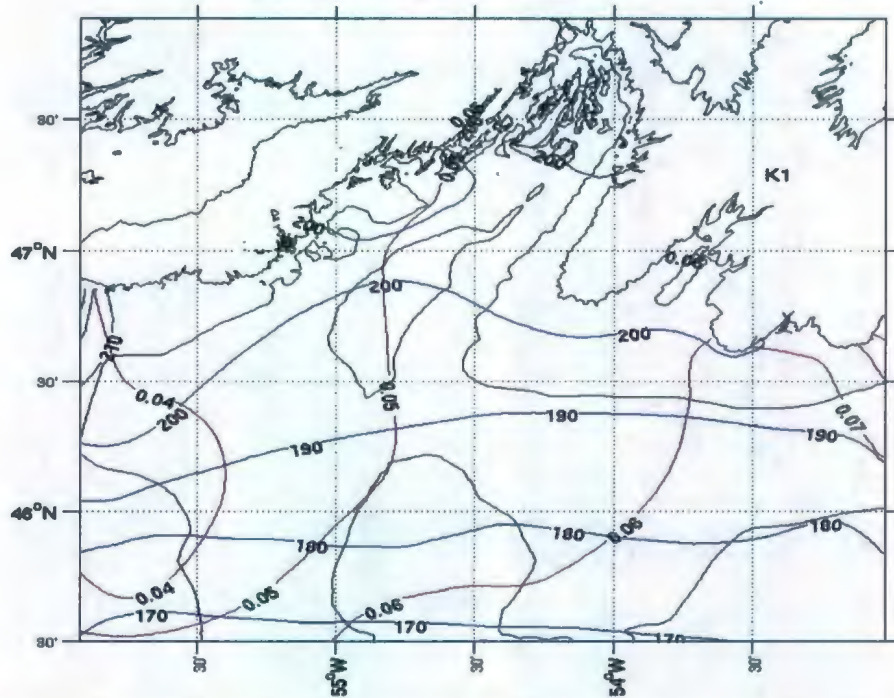


Figure 4-1: M_2 and K_1 coamplitude and cophase chart. Amplitude contour line is shown as red color and phase line is in blue color. 100 m and 200 m isobaths are displayed as a thin solid line.

Table 4-1.

Summary and statistics for observed and computed semidiurnal and diurnal tidal elevation and pressure gauge. AO is the amplitude of the observed site. PO is the phase of the observed site. AMO is the amplitude difference of observed and model results. PMO is the phase difference of observed and model results.

Sites	AO(<i>cm</i>)	PO($^{\circ}$)	AMO(<i>cm</i>)	PMO($^{\circ}$)	RMS amplitude difference(<i>cm</i>)	RMS phase difference($^{\circ}$)	absErr(<i>cm</i>)	relErr
M_2								
NF-8	67	334.4	-2.2	-1.05	2.85	1.92	2.47	3.62%
NF-9	69	338.8	-3.38	2.49				
S_2								
NF-8	19	14	-1.81	-2.4	2.83	4.39	2.1	10.7%
NF-9	20	15.8	-3.57	5.84				
N_2								
NF-8	13	321.5	-0.27	-7.21	1.39	5.18	1.28	9.1%
NF-9	15	324.1	-1.94	-0.32				
K_1								
NF-8	9	179.7	-3.8	21.58	3.02	19.18	2.53	30.9%

NF-9	7	183.2	-38	1643				
O_1								
NF-8	8	170.8	>>>	-1.38	8.24	2.18	2.09	35%
NF-9	8	165.4	<<<	1.96				

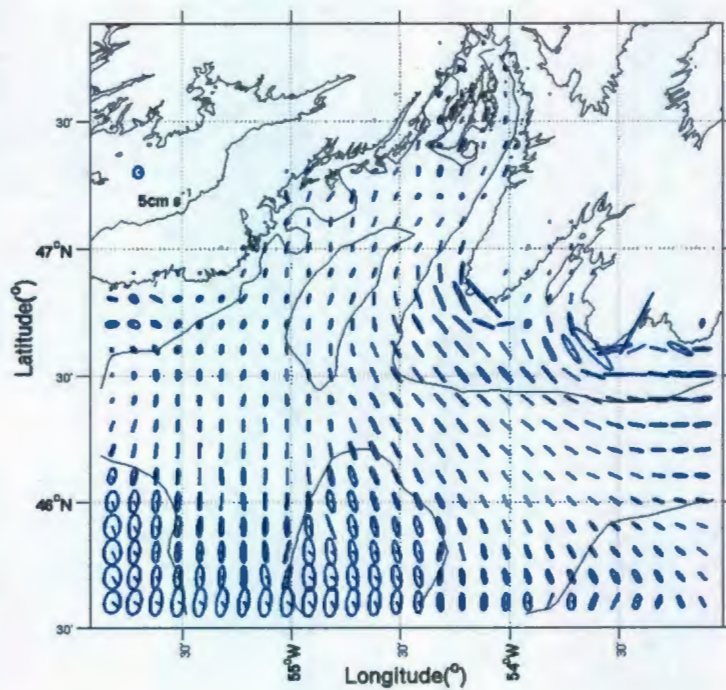
4.2 Tidal Currents and Comparison

The computed M_2 tidal current ellipses at the sea surface layer ($\sigma = 0.005$) and the twentieth layer ($\sigma = 0.995$) are shown in figure (4-2) (a) (b). A nearly rectilinear tidal flow (10 cm/s) dominates the Avalon channel and along the coast of Avalon Peninsula. In the outer bay, the tidal flow has a magnitude of $3\text{-}5 \text{ cm/s}$. The tidal current at the head of bay is weaker except near the coast. Relatively stronger tidal currents occur on the outer shallow banks, with amplitude approaching 10 cm/s ; the spatial pattern of the bottom tidal current ellipses (Figure 4-2 (b)) is similar to that of the surface current, but the magnitude of the bottom current is dramatically reduced by the bottom friction. The S_2 and N_2 tidal currents (not shown) have similar spatial patterns to the M_2 tidal constituent but with smaller magnitudes.

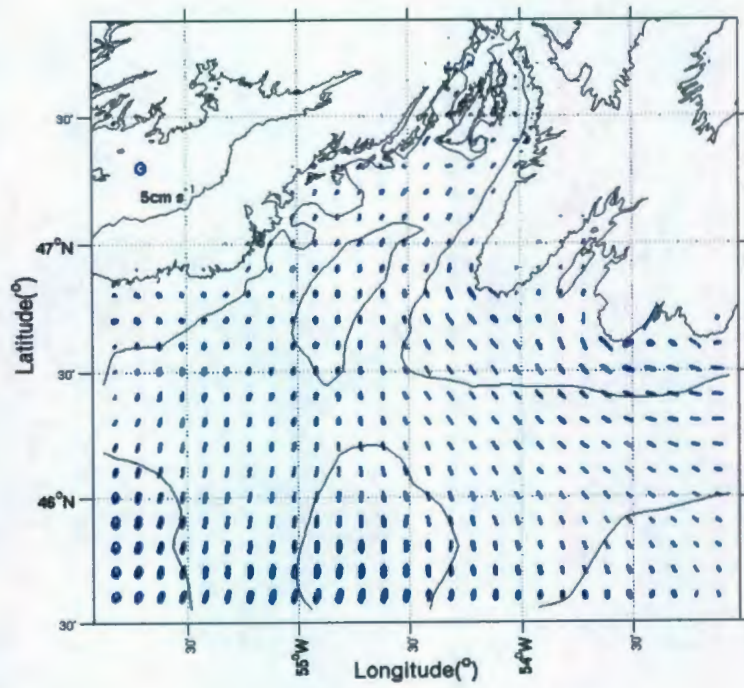
The computed K_1 tidal current at the sea surface is relatively weak compared to the M_2 tidal current (Figure 4-2(c)). The K_1 tidal current exhibits a zonal rectilinear flow pattern with decreasing in magnitude toward the west and the maximum one around 6 cm/s can be found in the outer shelf banks. The O_1 tidal current pattern is similar to that for K_1 (Figure 4-2(d)),

but with much smaller magnitude. Both the K_1 and O_1 bottom current magnitudes (not shown) are also reduced by bottom friction. The general surface current features in the present model are consistent with previous model results (Han, 2000)

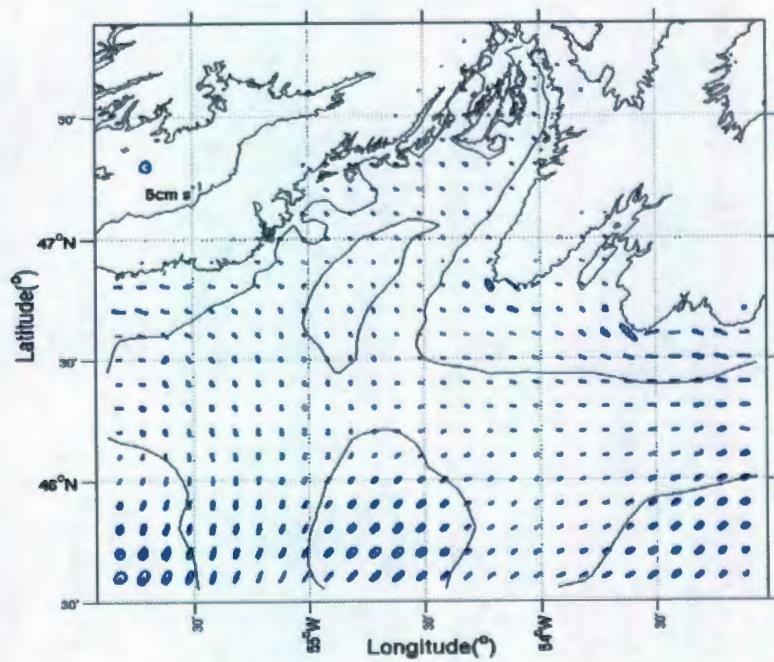
(a) M_2 at $\sigma = 0.005$



(b) M_2 at $\sigma = 0.995$



(c) K_1 at $\sigma = 0.005$



(d) O_1 at $\sigma = 0.005$

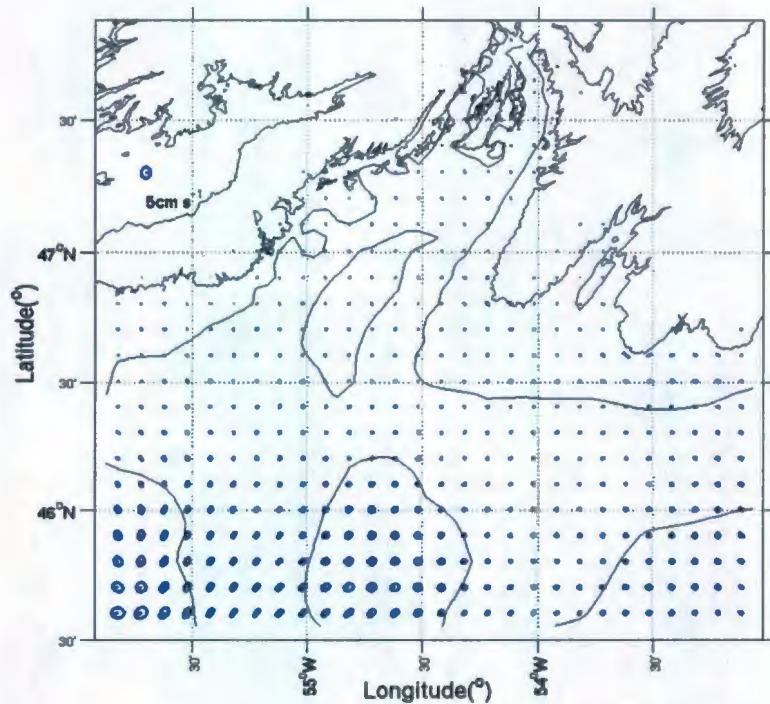


Figure (4-2): M_2 tidal current ellipses (a) near surface and (b) near bottom, and (c) K_1 , (d) O_1 current ellipses near surface. The 100m and 200m isobaths is displayed as a thin solid line.

The computed magnitude and phase for zonal and meridional components of the M_2 tidal constituents are compared with the moored current meter measurements (see Table 4-2). Currents of the other four tidal constituents current are too small and not considered for current comparison. Altogether, 7 points at different depth are available for comparison and the RMS difference of the M_2 tidal current between model results and observation data is 1.8 *cm/s* and 0.7 *cm/s* for the zonal and meridional

velocity respectively. The relative RMS_{error} reaches 40.4% and 32.4%. Scatter diagram for M_2 tidal current was shown in Figure 4-3 which indicates a good agreement in comparison, especially in meridional velocity. Large differences for some points in zonal amplitude were examined and may relate to the smoothed bathymetry.

Table 4-2.

Statistics of model computed currents for M_2 compared with the observation data

M_2	RMS_{error} U	RMS_{error} U	RMS_{error} V	RMS_{error} V
	Amp(<i>cm/s</i>)	Phase($^{\circ}$)	Amp(<i>cm/s</i>)	Phase($^{\circ}$)
	1.77	25.1	0.69	25.14
	absErr U(<i>cm/s</i>)	absErr V(<i>cm/s</i>)	relErr U	relErr V
	1.27	1.18	40.42%	32.37%

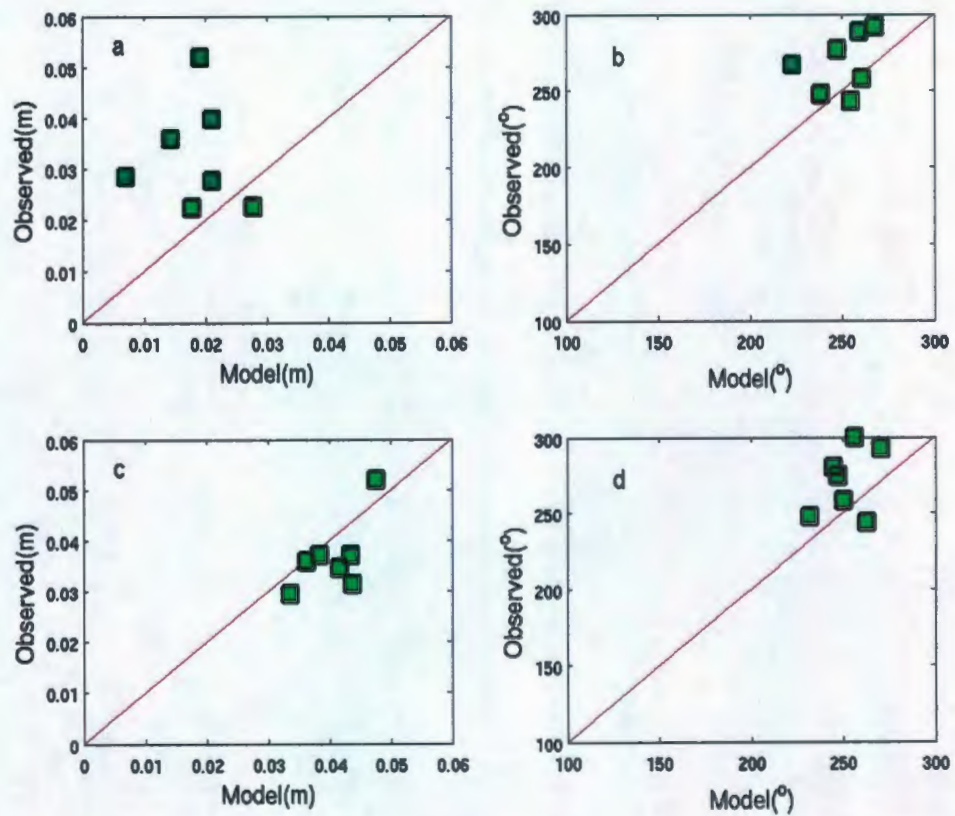
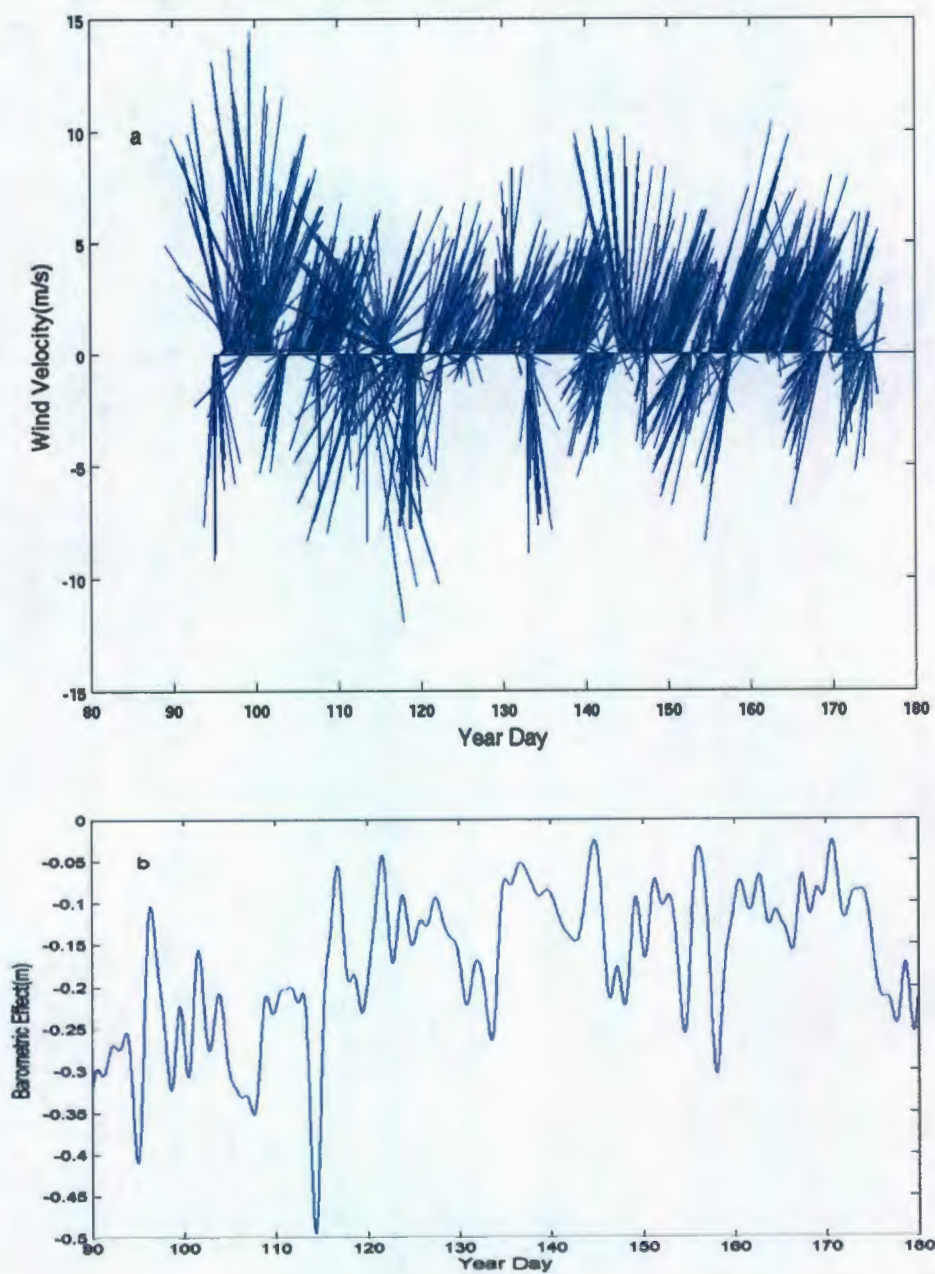
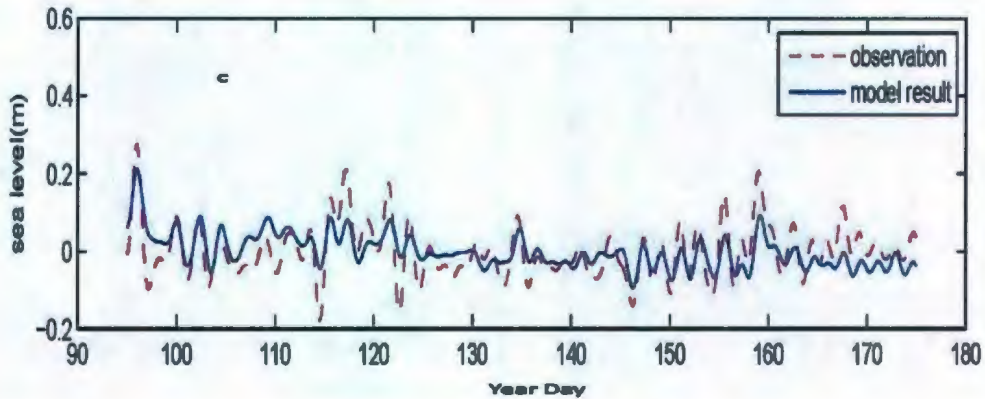


Figure (4-3): Scatter diagram of the M_2 tidal current amplitude and phase for zonal and meridional velocity. (a) amplitude of U. (b) phase of U. (c) amplitude of V. (d) phase of V

5 Current, temperature and salinity

5.1 Sea level comparison at Argentina





Figure(5-1): (a) wind forcing in Argentina,(b) inverse barometric effect from st.john's station air pressure data, (c) 36 hour low pass filtered sea level comparison.

A time-series comparison between hourly observed and modeled sea level is shown in Figure (5-1). We also plotted the hourly wind velocity vectors used to force the model (Figure5-1, a). The inverse barometric effect has been removed from the tide gauge data to enable comparison with the model sea level. There is a fair agreement in both amplitude and phase at this station, with the amplitude agreement best when the wind is strong. Thus, the sub-tidal sea level variations and the correlation with wind velocity vectors can be seen. From the day 110-120, the wind is upwelling-favorable at first and the sea level decreases to around -0.2 m; whereas when the wind changes to downwelling-favorable, the sea level increases to 0.2 m. Our model qualitatively reproduces this feature and the quantitative difference is probably from the inverse barometric effect generated from air pressure data in St.John' s airport instead of Argentina since there is no air pressure data

during the model running time.

Quantitative comparisons are also made for low pass filtered times series. The RMS difference between the observed and model sea level is 5.2 cm and γ^2 is 0.58 which demonstrates a relative reasonable agreement with the observed sea level.

5.2 Comparison of Observed and Simulated Temperature Values

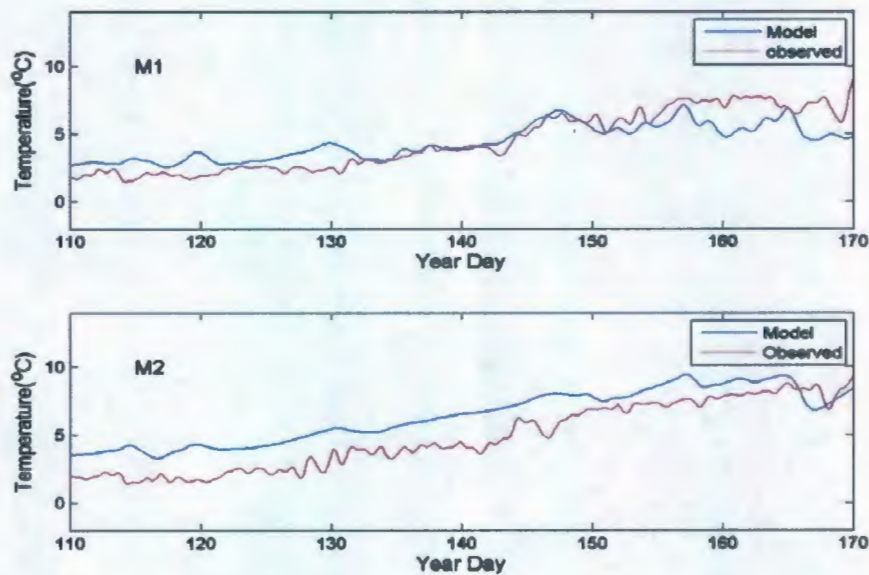
Both model and observed temperatures are shown in Figure 5-2, for M1-M6 at 10 m, 20 m, 30 m, 40 m, 55 m, 75 m, 80 m, 100 m. The model results correctly display the seasonal temperature variability at upper layer of the water column. The largest hourly difference between the observed and computed temperature value is about 4 °C . Averaged over 24 hours, the difference is reduced to around 2.6 °C . Upper ocean temperature values range from 2 °C at the beginning to 8 °C at the end and is highly variable, especially in June. In contrast, the temperature at depths greater than 30 m was much less variable. Overall the model results agree well with seasonal observation. In the deeper ocean, model results present a decreasing trend in temperature which is consistent with the observational data, due to the low temperature inflow from the Labrador inshore flow.

We note that the temperature fluctuations at M4 from days 147-160

show strong variability, even at 40 and 45 m. A temperature jump of about 7 °C can be seen which may be due to the two strong and opposite direction wind during this period Figure5-1(a). The relation between the wind and temperature can be explicitly seen from wind time series. When the wind blows from northeast, the surface warm water will transport from the west to the east of the Bay, making the surface water mix down into the water column and leading the deepwater temperature to increase on the eastern bay. We can also roughly check the wind time series around day 146; the wind starts to blow northeasterly, then the temperature increase can be found at M4, especially at 40 and 45m. Therefore, when the wind blows southward, the temperature is expected to decrease at 40 and 45m along eastern Bay and the corresponding feature exists in Figure 5-2 (h,j) . Here, we also need to mention another important aspect affected the temperature fluctuation. As mentioned in Chapter 2, the cold trapped water inflow will come in through the open boundary and then pass M4. From the temperature transect in Figure 5-4, a cold mid layer can be found which will also affect the temperature at 40 m and 45 m at M4. These high frequency time-scale temperature variations are also associated with the M4 depth which is only 51m and easier to mix down. This can be examined by the close point M3

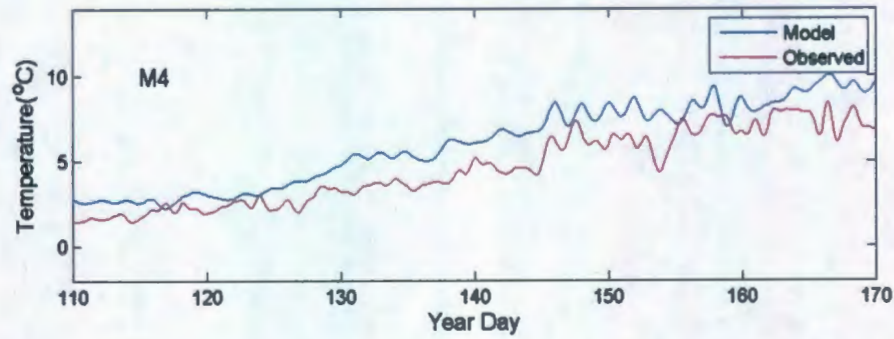
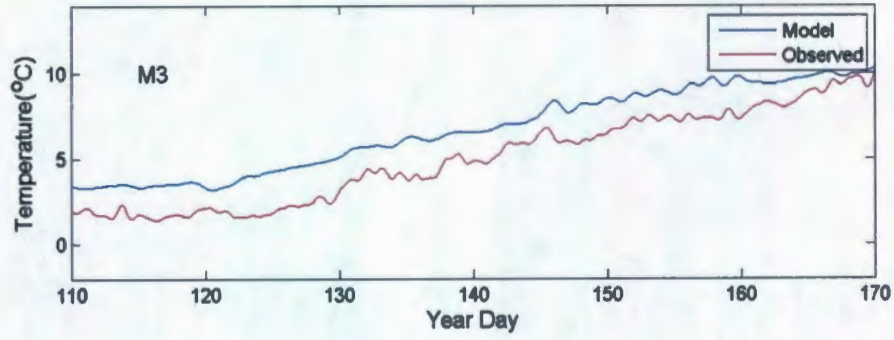
which is around 100 meters deep. For M3 temperature time series, strong variability can be hardly found during early summer time. With the above temperature fluctuation at M4, our model indeed demonstrates reasonable skill in producing these synoptic time-scale features at this site and performs well during day 147-160.

(a) 10 m

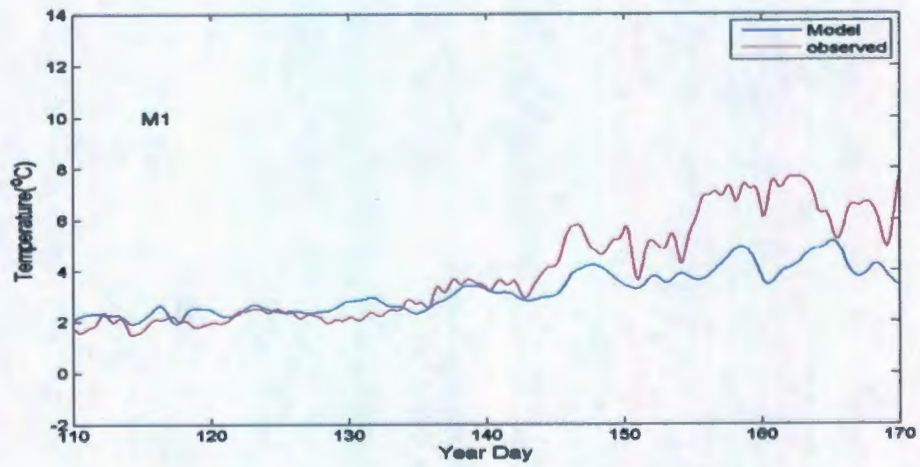


Figure(5-2): Time-series temperature comparison of filtered(36-h low-pass filter) observed(red line) and simulated(blue line) for six points at different depths (a)observed and model temperature for M1 and M2 at 10 m.(b) observed and model temperature for M3 and M4 at 10 m .(c) observed and model temperature for M1 at 20 m (d) observed and model temperature for M3 and M4 at 20 m (e) observed and model temperature for M1 and M2 at 30 m (f) observed and model temperature for M3 and M4 at 30 m (g) observed and model temperature for M1 and M2 at 40 m (h) observed and model temperature for M3 and M4 at 40 m (i) observed and model temperature for M1 and M2 at 55 m (j) observed and model temperature for M3 at 55 m and M4 at 45 m (k) observed and model temperature for M5 and M6 at 75meter(l) observed and model temperature for M2 and M3 at 80 m (m) observed and model temperature for M2 at 100 m.

(b) 10 m

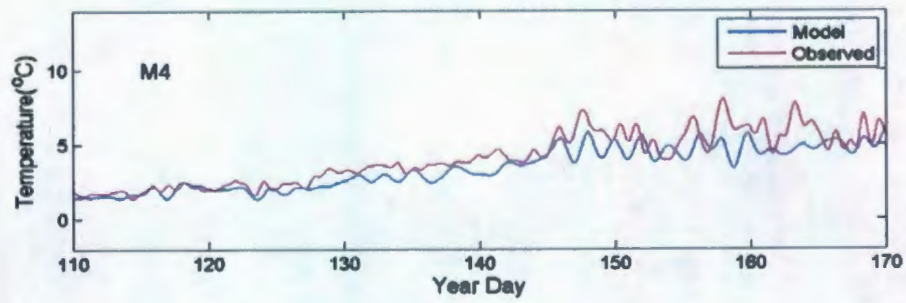
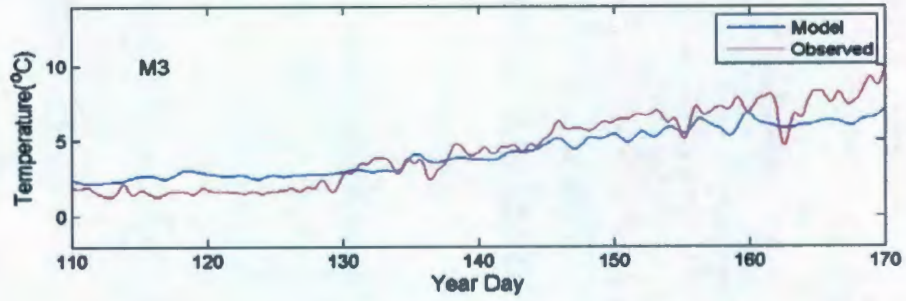


(c) 20 m

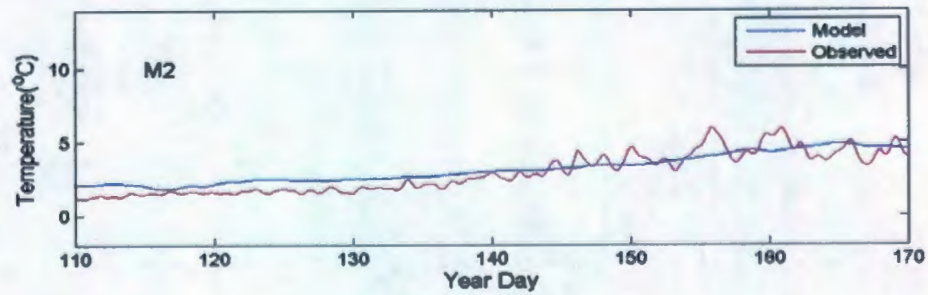
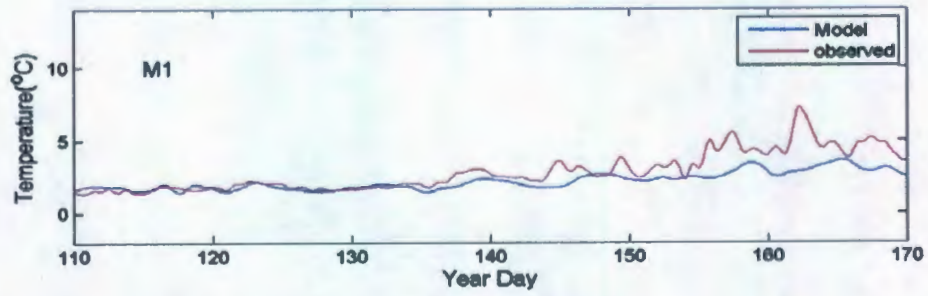


(Continued)

(d) 20 m

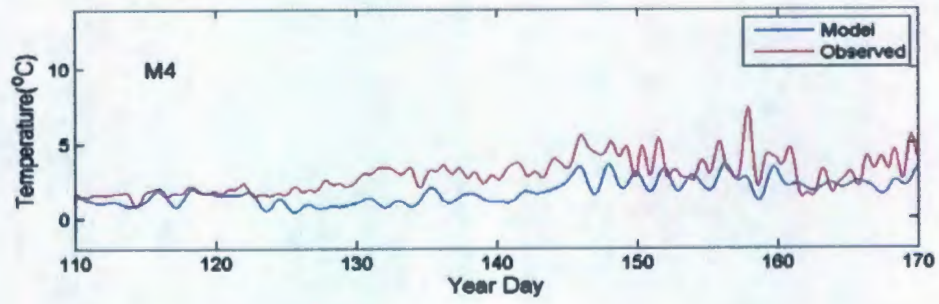
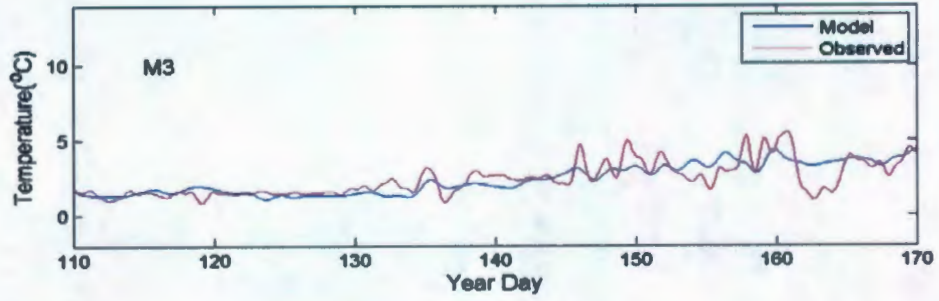


(e) 30 m

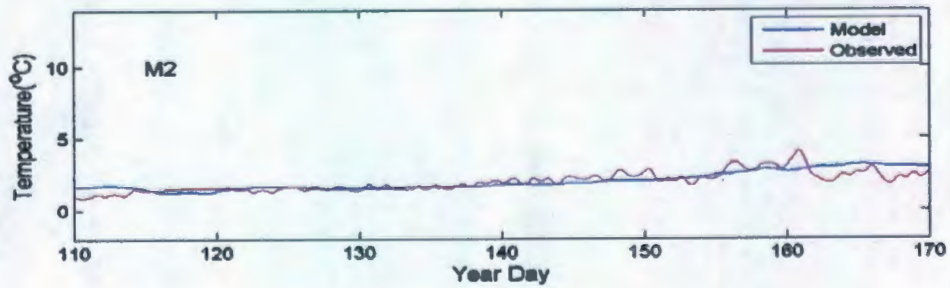
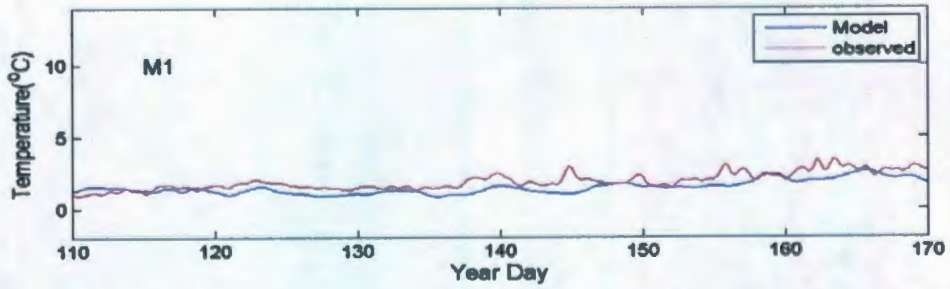


(Continued)

(f) 30 m

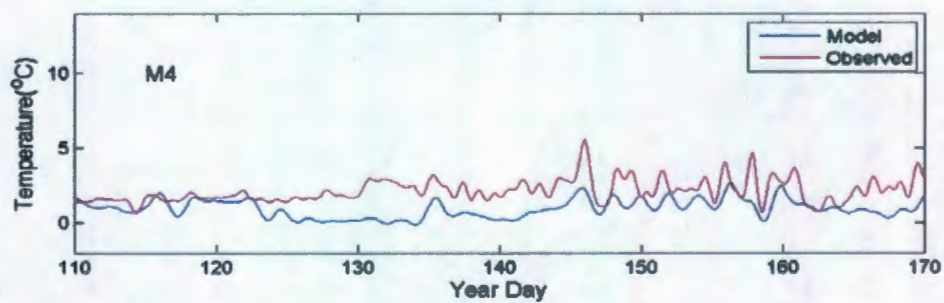
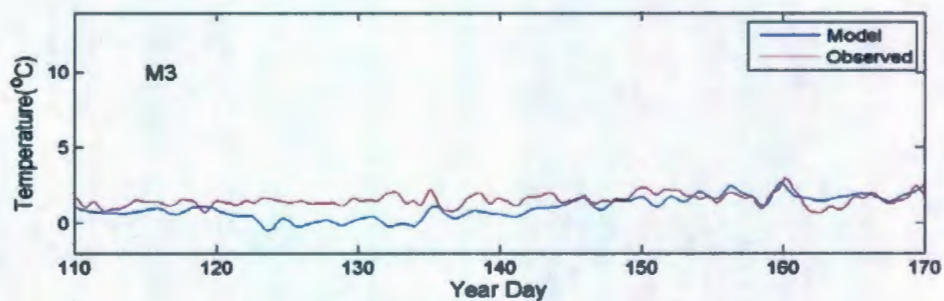


(g) 40 m

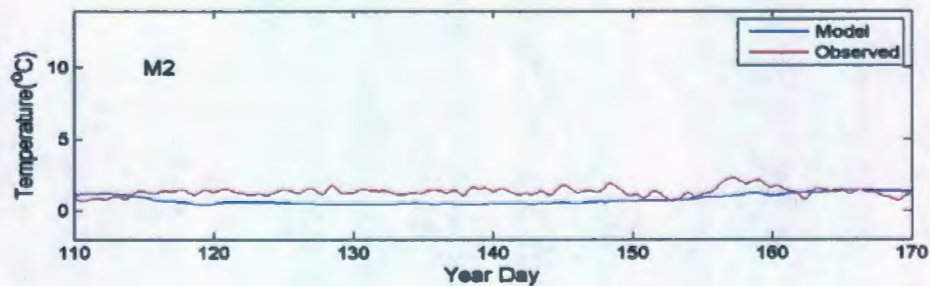
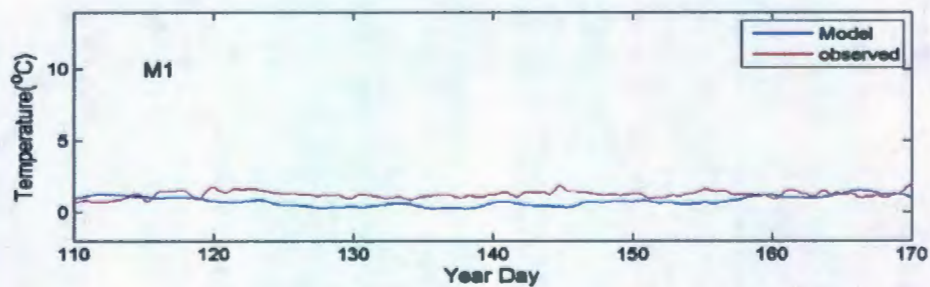


(Continued)

(h) 40 m

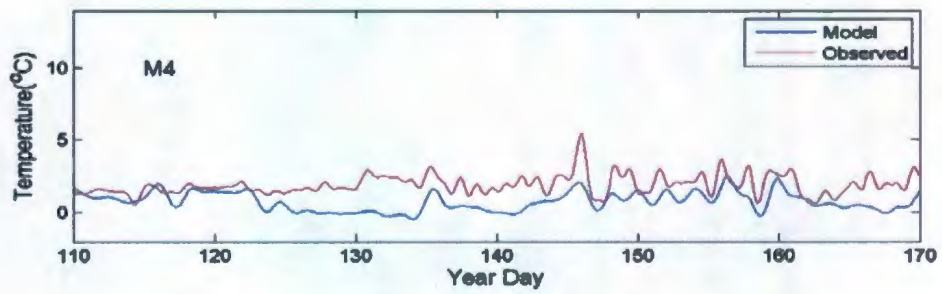
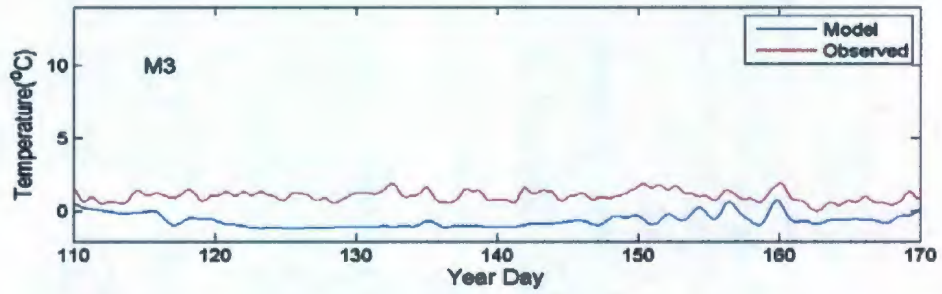


(i) 55 m

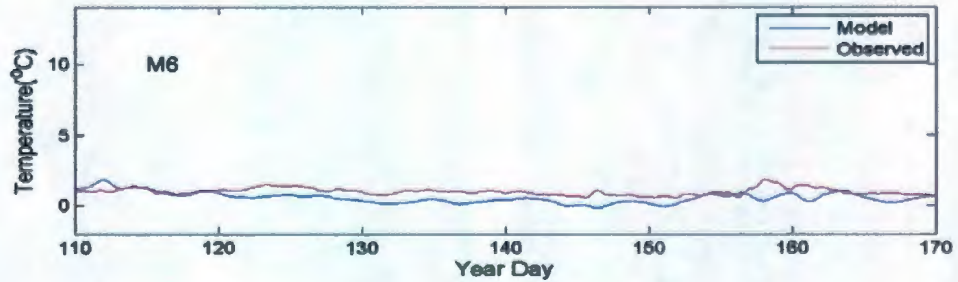
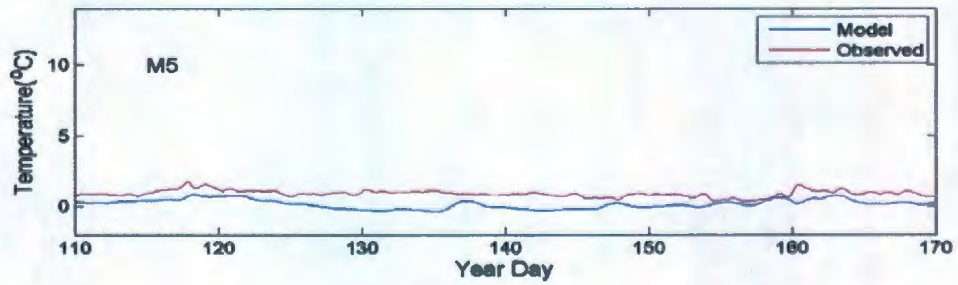


(Continued)

(j) 55 m and 45 m(M4)

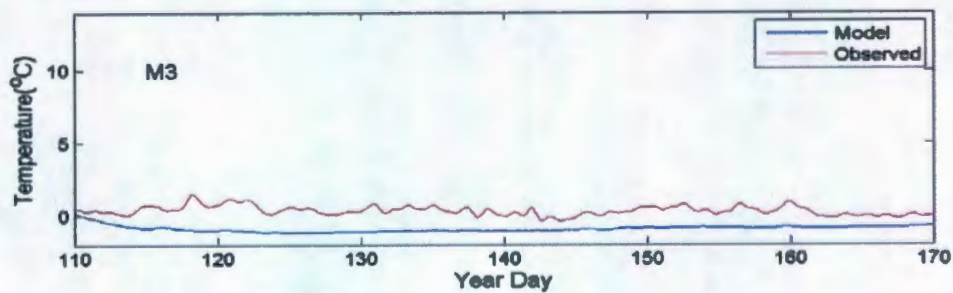
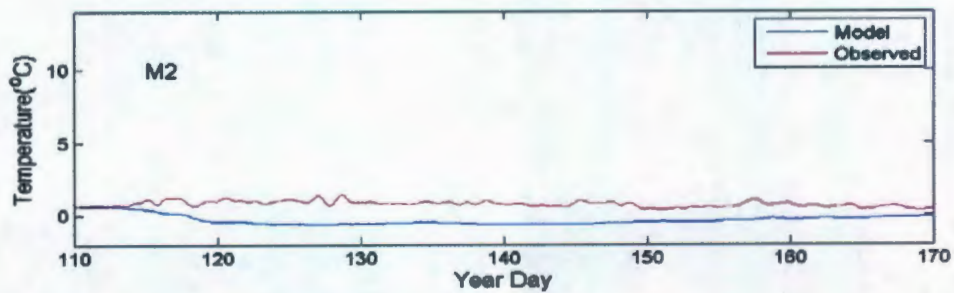


(k) 75 m

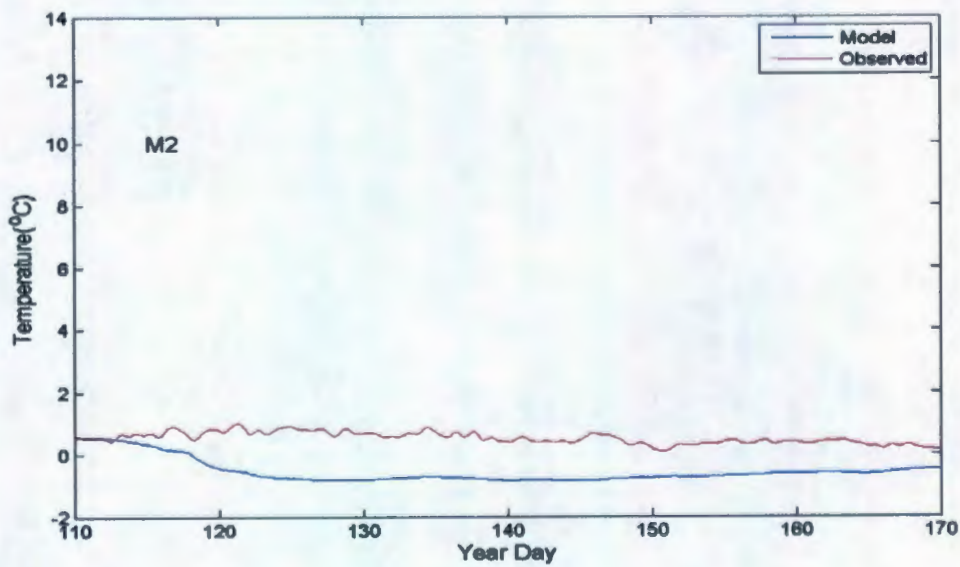


(Continued)

(l) 80 m



(m) 100 m



(Continued)

Quantitative comparisons are made and summarized in Table 5-1 to 5-4, respectively, for low pass filtered temperature times series. RMS difference, γ^2 and the correlation coefficient used for quantifying the agreements between the observed and model time series temperature. Considering the seasonal trend in the upper ocean, we separate the temperature statistics into two parts: above 30 m and below 30 m. We define a comparison to be good for the upper 30 m when the RMS difference is around 1 °C and γ^2 is less than 1. If γ^2 is less than 0.5, the model results are treated to be at very good comparison. Considering the small variation in temperature time series in deeper water, we only calculate the RMS difference to determine the bias of the model results. This difference is then treated as an only indicator to determine if the comparison is good or not. X stands for no data in observation or model results.

As can be seen (Table 5-1 to 5-3), the RMS_{error} at the upper 30 m is around 1 °C and γ^2 for upper 30 m is below 1 except M4 at 30m which indicate a good comparison. We also did data regression analysis and determined the correlation coefficient between the model and observed temperature at these depths which is around 0.9 with a high correlation of 0.98 for M3 at 10 m. The relative poor comparison for M4 at 30 m may be

because of smoothed depth which leads to the shift of the value against to the observation. The deeper water temperature statistics at M1-M6 are also examined and the RMS_{error} difference ranges from 0.5 to 1.7 °C which is a relatively good comparison. The temperature comparison statistics demonstrates overall good agreement between the observed and calculated results. Such good agreement at different depths suggest that our model strategy for Placentia Bay is justified in temperature, including the manner in which we specify the surface net heat flux and shortwave heat flux. Further improvement will require higher resolution time dependent weather condition to replace the six-hourly heat flux forcing for calculating the small time scale temperature features and spatial dependent wind or the use of data assimilation. For our purpose, however, data assimilation is not desirable since our goal is to understand from the seasonal temperature to synoptic time scales, requiring mass conservation over entire model simulation time.

Table 5-1

Statistics for 10 m model-observation temperature comparison at M1, M2, M3, and M4

Points	RMS_{error} (°C)	γ^2	Correlation coefficient
M1	1.22	0.32	0.87

M2	1.79	0.55	0.94
M3	1.73	0.44	0.98
M4	1.58	0.57	0.95

Table 5-2

Statistics for 20 m model-observation temperature comparison at M1, M2, M3, M4

Points	RMS_{error} (°C)	χ^2	Correlation coefficient
M1	1.48	0.58	0.9
M2	X	X	X
M3	1.07	0.2	0.96
M4	0.99	0.35	0.9

Table 5-3

Statistics for 30 m model-observation temperature comparison at M1, M2, M3 an M4

Points	RMS_{error} (°C)	χ^2	Correlation coefficient
M1	1.07	0.72	0.83
M2	0.67	0.27	0.90
M3	0.74	0.49	0.72
M4	1.45	1.72	0.59

Table 5-4

RMS temperature difference between the observed and simulated value for six sites at 40 m, 55 m, 75 m, 80 m, and 100 m.

RMS_{error}	40	55 m)+5 m	75	80	100

	$m(^{\circ}C)$	for M4)($^{\circ}C)$	$m(^{\circ}C)$	$m(^{\circ}C)$	$m(^{\circ}C)$
M1	0.57	0.62	X	X	X
M2	0.43	0.70	X	1.16	1.14
M3	0.84	1.74	X	1.30	X
M4	1.44	1.38	X	X	X
M5	X	X	0.82	X	X
M6	X	X	0.57	X	X

5.3 Comparison of Observed and Simulated Vertical Temperature

(a)

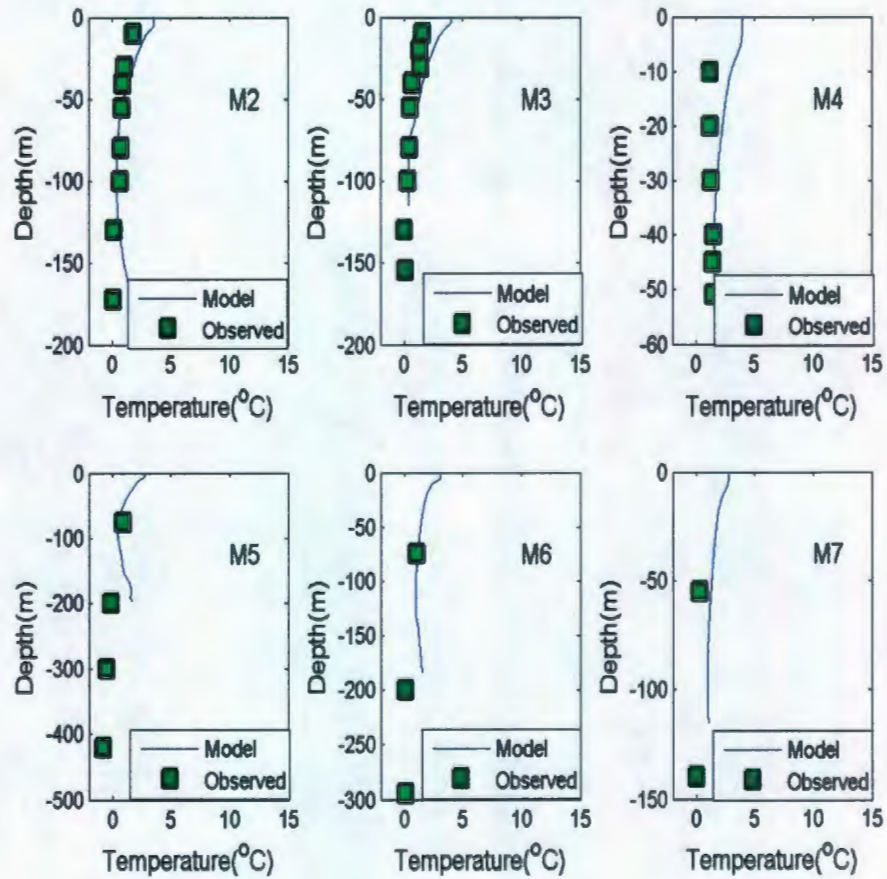
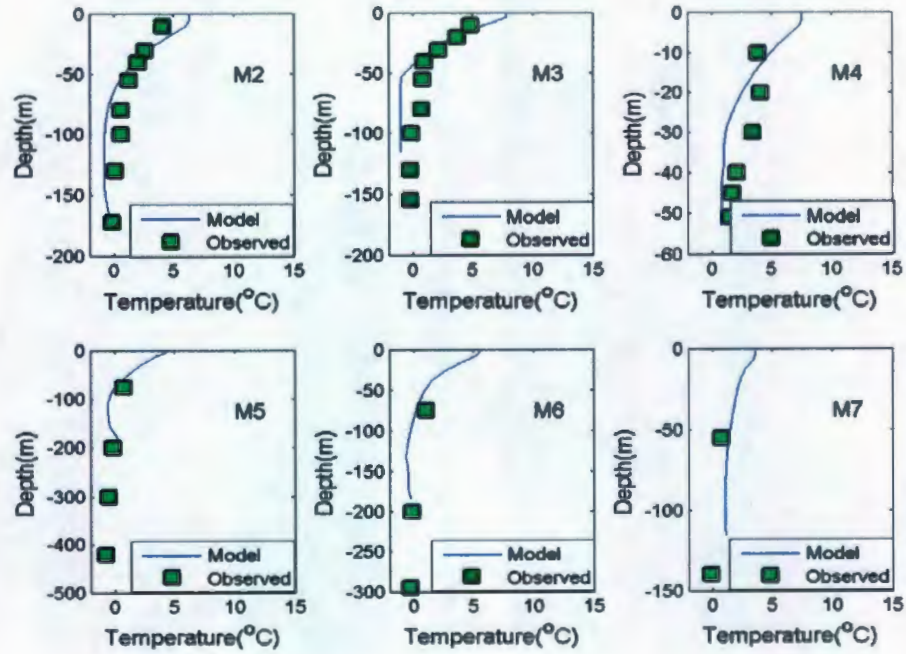
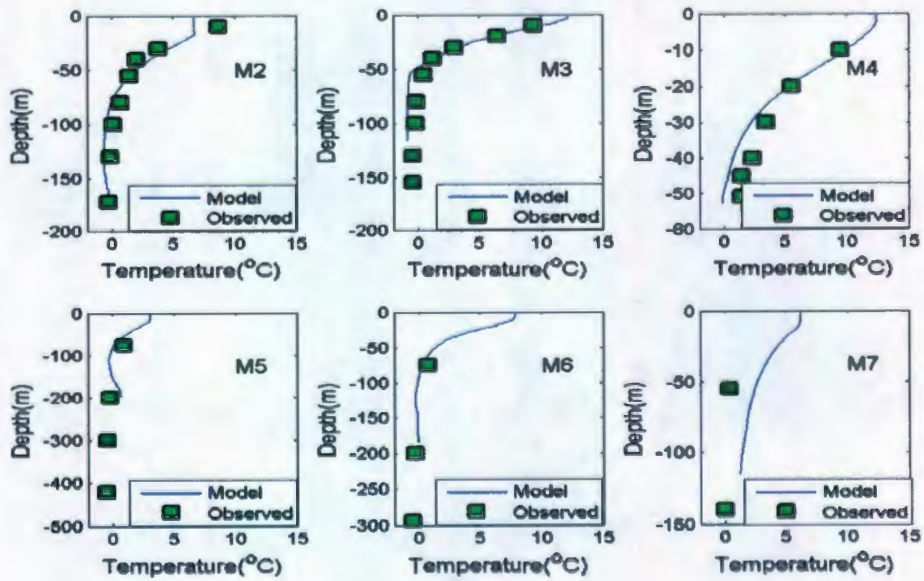


Figure (5-3) Comparison of the vertical temperature profile between the model results and observation for the six points on (a) April 15, (b) May 1, (c) June 15.

(b)



(c)



(Continued)

Figure 5-3 shows the comparison of the vertical temperature profile between the model results and the observation data at the middle of April, May and June, respectively. Fair agreement with the observed data can be found in general. There is approximate agreement in the thermocline formation and evolution from spring to summer time. In spring, temperature is more uniform from surface through deep water with the surface temperature below 5 °C. In summer, with the increasing temperature at the top 50 m, the thermocline layer can be clearly observed and surface temperature difference at different sites occurs. Surface temperatures at M4 and M3 are 5 °C higher than at M2 probably because of the coastal upwelling on the west side of the Bay.

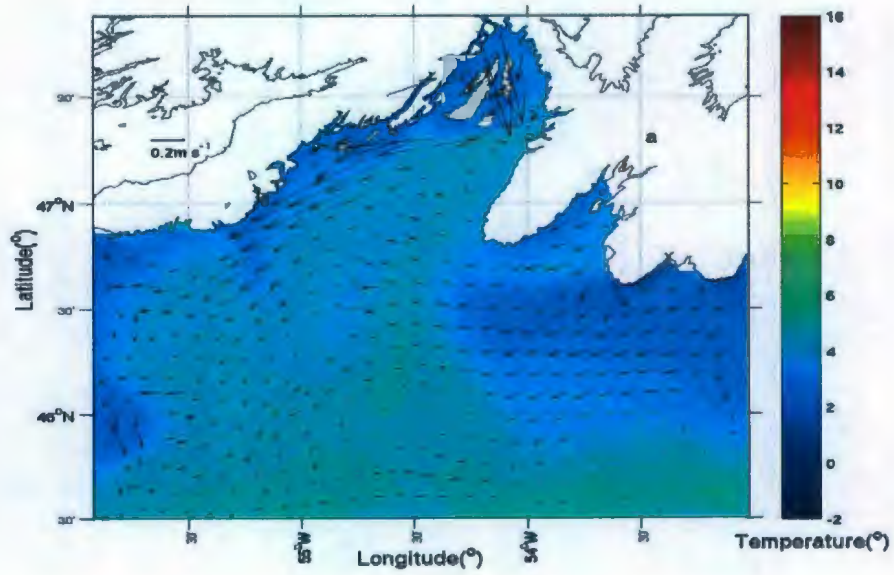
5.4 Seasonal Surface Temperature Pattern

The model reproduced two distinct circulation modes that reveal the differences in wind forcing from spring to summer season (Figure 5-4). During spring, the winds were generally southerly at first and then changed to northerly by the middle of the April. Here, we select the time after the middle of April. As a result, surface currents flowed westward along the coast (Figure 5-4 (a)). During June, upwelling along the west coast was generated by the strong southerly winds due to the Ekman flow (Figure 5-

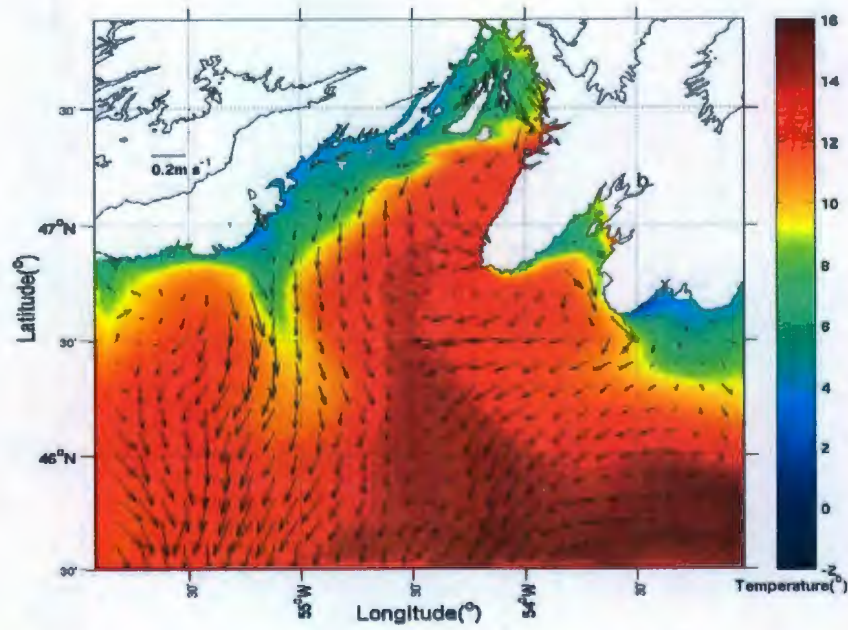
4(b)).

The simulated surface temperatures from Placentia Bay were consistent with the general circulation patterns. The lower temperature water spread westward along the coast during spring time. On April 19, northerly winds pushed the cold water from east coast into the inner Bay and further to the west along the west coast. Then a cold water layer around 0 °C occurred. In contrast, on June 15, southwesterly winds pumped the low temperature water from deeper layer onto surface along west coast. This offshore transport of low temperature water was most notable near 47 °N where a pool of low temperature water is observed (Figure 5-4(b)). As the cold water spread southeast to contact with the warm water there, a cold water front formed and consequently, a thin layer with a gradient of 9 °C over 100 km occurred between the warm and cold water. As a result of the southwesterly winds, surface temperature along the east coast warmed.

(a)



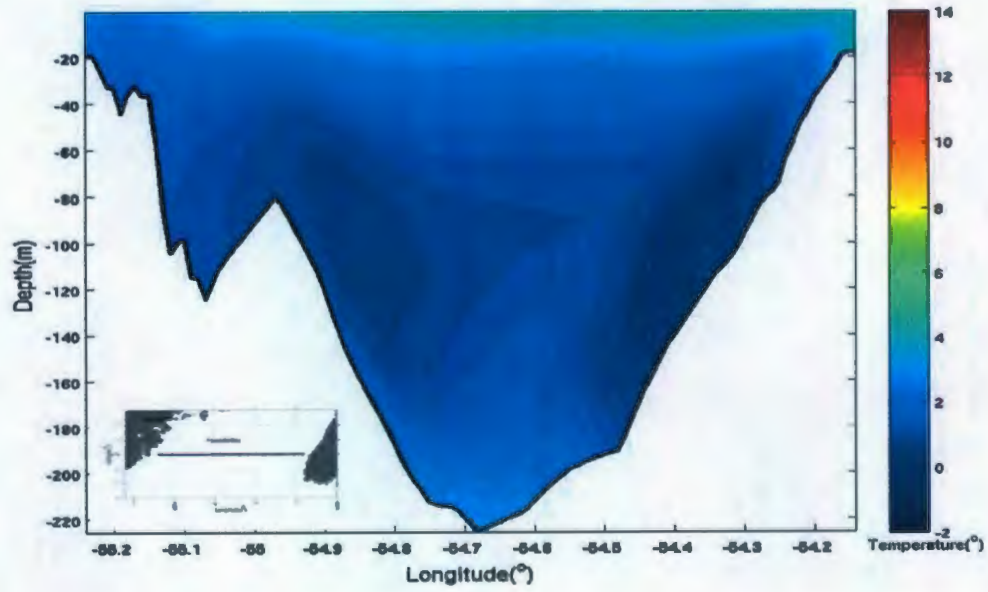
(b)



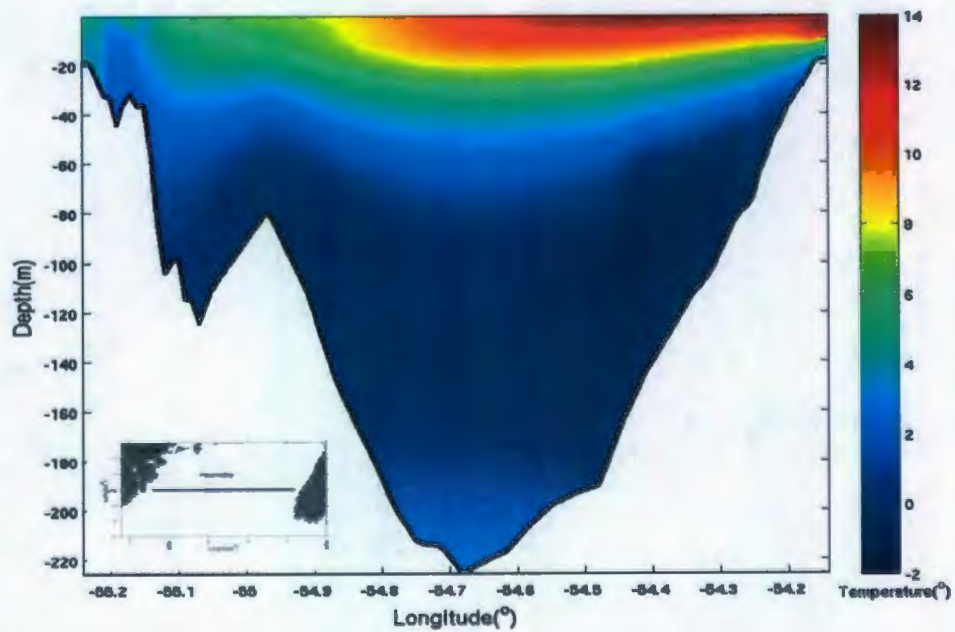
Figure(5-4): Surface circulation and temperature surface field at two different times for (a):April-19-18:00 and (b): June-15-0:00

We also showed the temperature along $47^{\circ}N$ transect under the real forcing (Figure 5-5). To examine the seasonal pattern of the temperature profile along this transect, we select two times in April and June. The early spring temperature transects shows cold water at the surface and warm water trapped at the bottom of the deep basin in the center of the Bay. The middle part is the cold intermediate layer around $-1^{\circ}C$. Although the stratification is weak and the water column temperature is nearly uniform from the west coast to 100 m, this transect suggests weak upwelling on the western side and warmer water on the eastern side. The temperature pattern changes during the early summer. Temperature on the eastern side exhibits sharp thermocline and surface temperature reaching $13^{\circ}C$.

(a)



(b)



Figure(5-5): temperature transect along the 47 degree at two different time point (a):April-19-18:00 and (b) June-15-0:00.

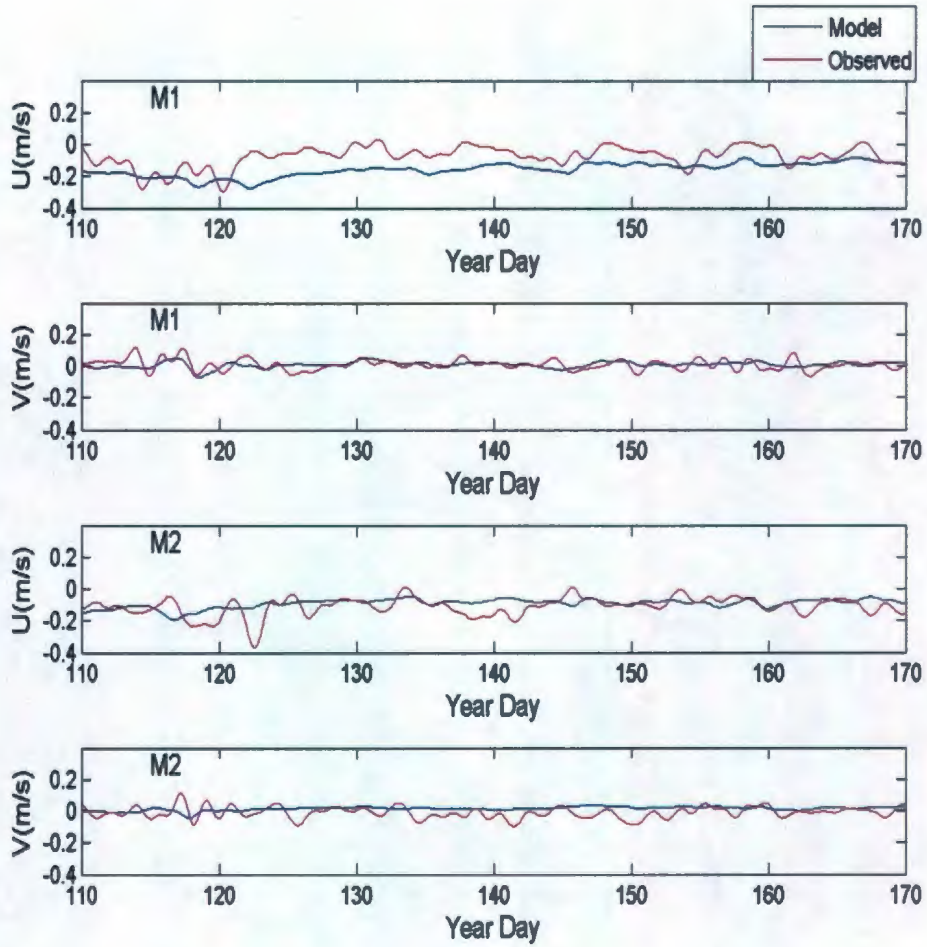
5.5 Time Series Comparison of Currents

In 1999, four current meter moorings were deployed across the outer portion of Placentia Bay. The current meter data provide important quantitative information of the circulation in Placentia Bay. For the simulation period, Currents at 20m and 55m were available for compared. All data were analyzed for flow at sub-tidal frequencies.

The rotated model and the observed (Figure 5-6) velocity are shown for two depths: 20 m and 55 m (45 m for M4). Here, we treat U as the along bay component and V as cross bay component. From the model, we sample the low pass filtered current data at the σ -layer most closely matching the data sample depth since the current model employs a σ -coordinate in the vertical. Figure 5-6 show that the alongshore component at these four stations are much stronger than the cross shore component and the velocity of the alongshore component decreased a little bit with depth. Then, we define a good comparison when model qualitatively reproduce the most feature of the observation and VDR is less than 1. As with the temperature and salinity the visual comparison for the hourly velocity components time series are quite good overall for M3 and M4. Quantitatively, The VDR and SDR at M3 and M4 are 0.31, 0.65 and 0.24, 0.5 at 20 m respectively (Table

5-5 to 5-6) which indicate a good comparison at 20 m for M3 and M4. However, we still find some relatively poor comparison at M1 and M2 and the maximum RMS difference can reach 10 *cm/s* with 1.1 for VDR at 20m at M1 (Table 5-5). Considering the location of these four points, M1 and M2 are located on the west side of the Bay and the currents are partially influenced by inner bay due to the cyclonic circulation over the Placentia Bay. Therefore, further improvement may require including the river discharge at the head of bay since we found the river discharge can reach 200 *m³/s* during May in 1999 (Environment Canada) and more grids in the areas where depth changes rapidly. The river discharge will change the vertical and horizontal salinity distribution of the inner bay and further influence the baroclinic response of the current field over the inner bay.

(a) 20 m



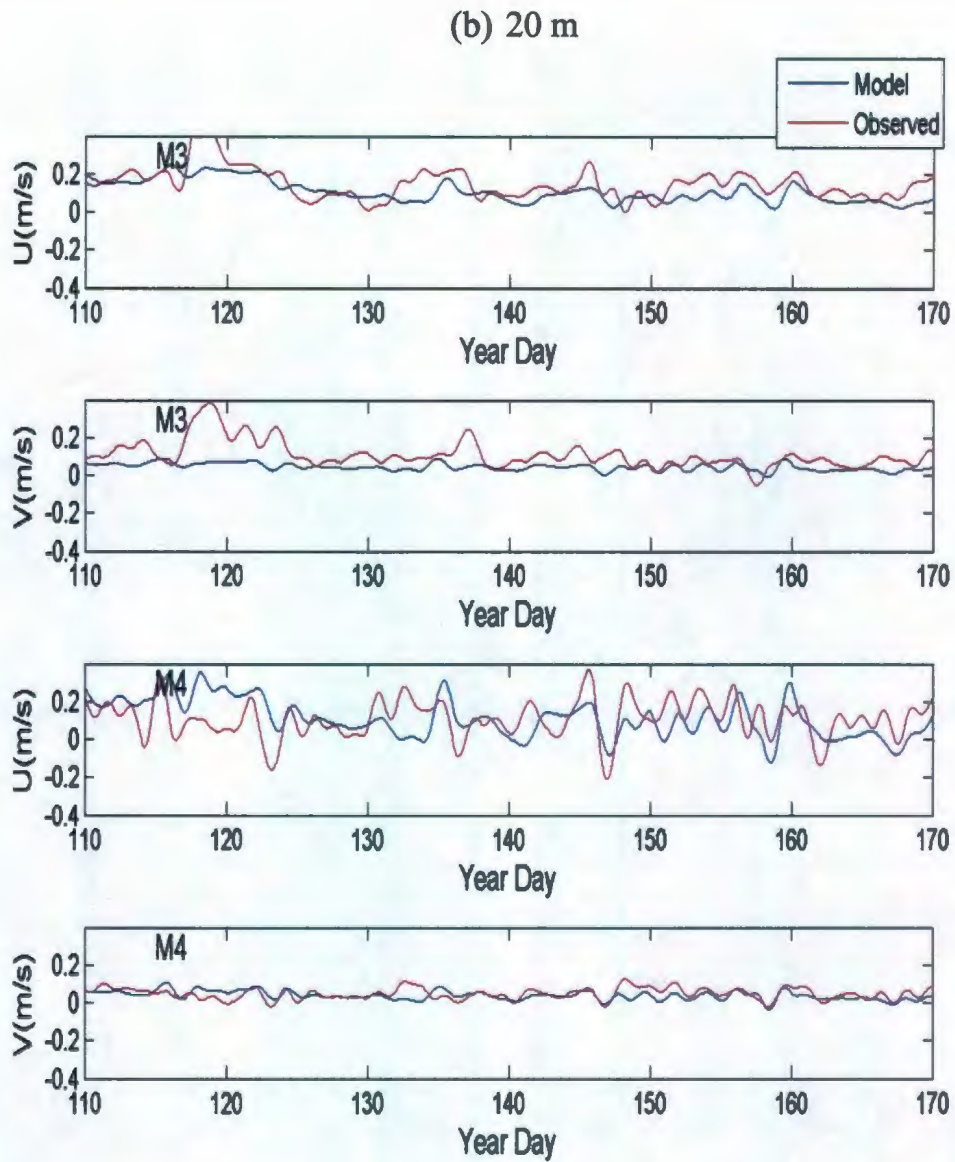
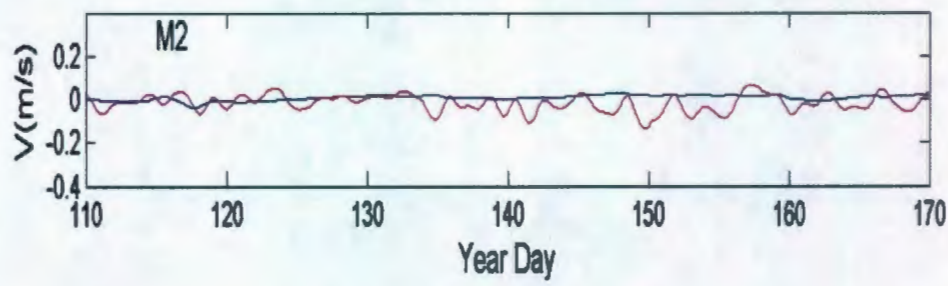
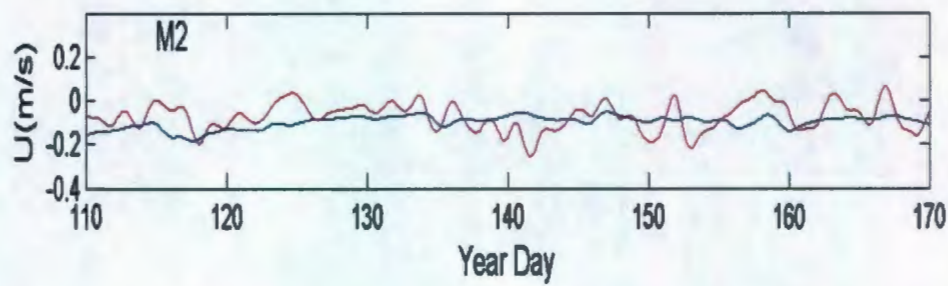
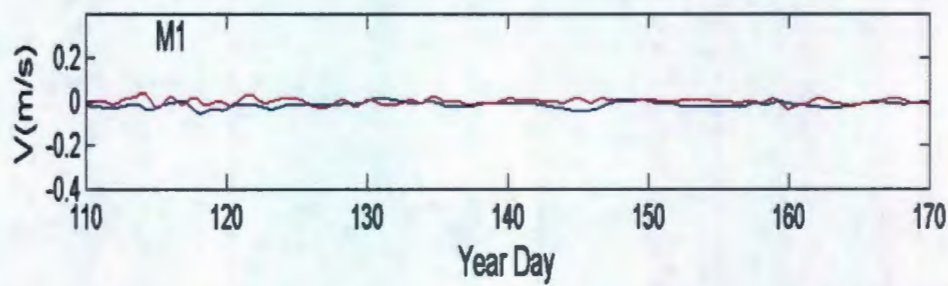
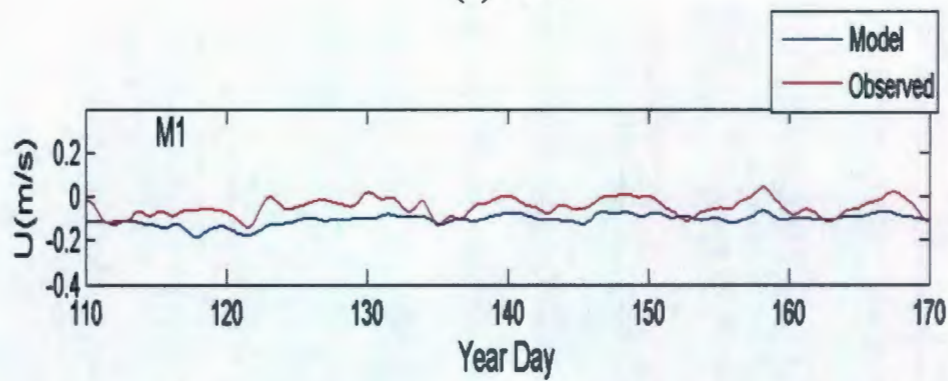


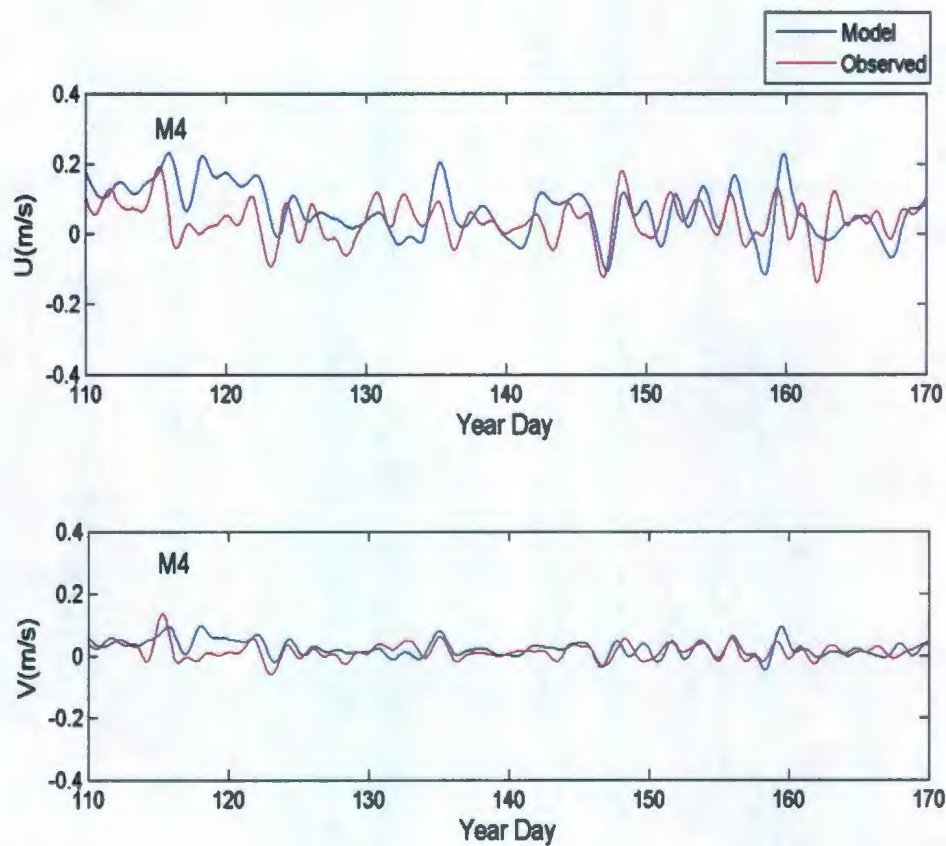
Figure (5-6): Time-series currents comparison of filtered (36-h low-pass filter) observed (red line) and simulated (blue line) for four points at different depths. (a) observed and model along bay and cross bay currents for M1 and M2 at 20 m (b) observed and model along bay and cross bay currents for M3 and M4 at 20 m (c) observed and model along bay and cross bay currents for M1 and M2 at 55 m (d) observed and model along bay and cross bay currents for M4 at 40 m

(c) 55 m



(Continued)

(d) 45 m



(Continued)

Table 5-5

Statistics for along bay and cross bay currents for four points at 20m. VDR and SDR index are calculated for currents.

	RMS error(m/s)	VDR	SDR
M1 along bay velocity	0.1	1.0	0.73
M1 cross bay velocity	0.03		

M2 along bay velocity	0.06	0.34	0.22
M2 cross bay velocity	0.04		
M3 along bay velocity	0.07	0.31	0.24
M3 cross bay velocity	0.09		
M4 along bay velocity	0.12	0.65	0.5
M4 cross bay velocity	0.03		

Table 5-6

Statistics for along bay and cross bay currents for four points at 55m. VDR and SDR index are calculated for currents.

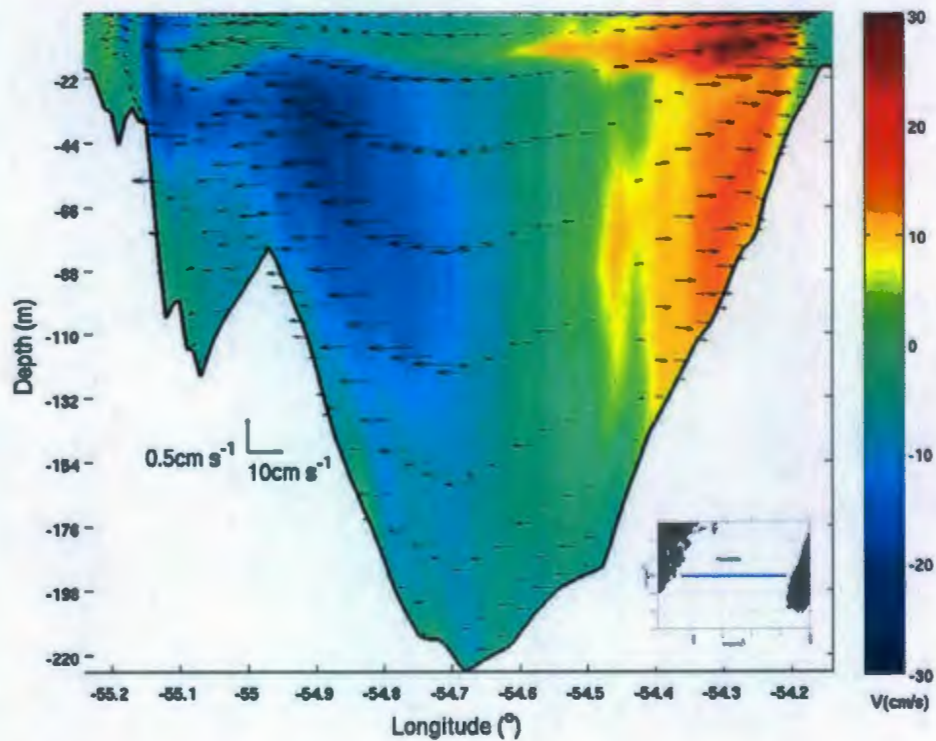
	RMS error (<i>m/s</i>)	VDR	SDR
M1 along bay velocity	0.06	1.1	0.89
M1 cross bay velocity	0.02		
M2 along bay velocity	0.07	0.65	0.34
M2 cross bay velocity	0.04		
M3 along bay velocity	X	X	X
M3 cross bay velocity	X		
M4 along bay velocity	0.07	1.3	0.9
M4 cross bay velocity	0.02		

5.6 Vertical Currents Section

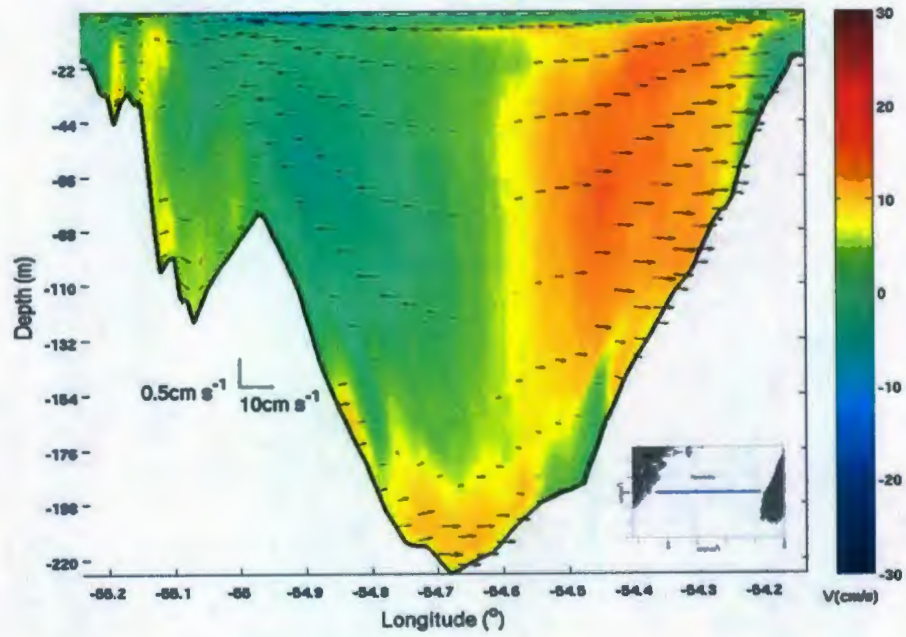
We examined the vertical temperature profile along 47 °N during the model run period. As shown in the Figure 5-7, vertical currents at three

different time all suggest the dominant flow is northward along the eastern side of the bay and southwards flow along the western side of the bay. These opposed flows can be explicitly seen in these three graphs. Except the near surface and bottom, a thin static layer occurs between the opposite direction flow. These two flows also indicate the seasonal variability probably caused by the seasonal transport. The northward flow is extremely strong in spring and becomes weak as summer progresses. The southward flow shows a similar seasonal scale.

(a)



(b)



(c)

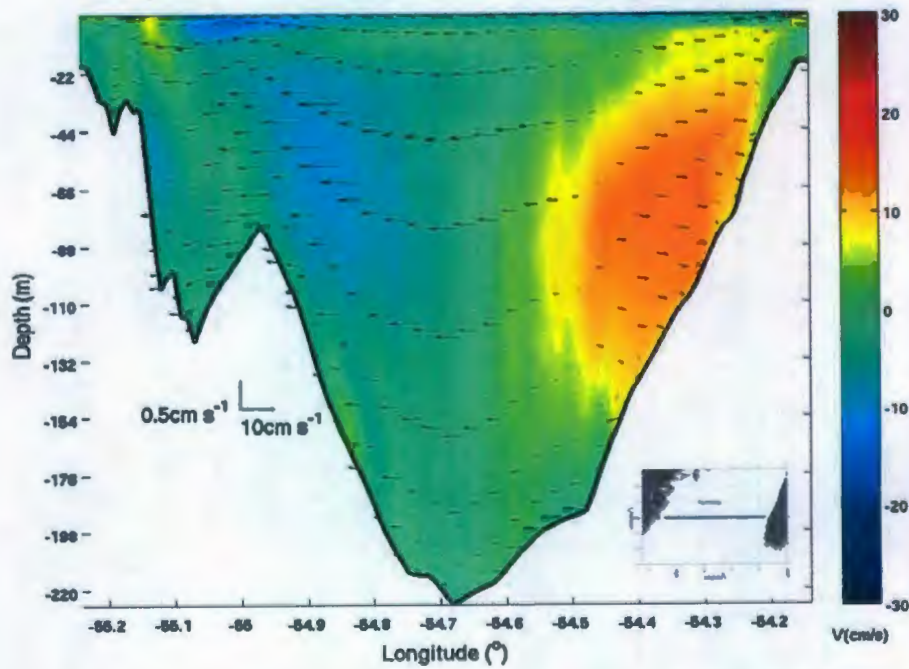
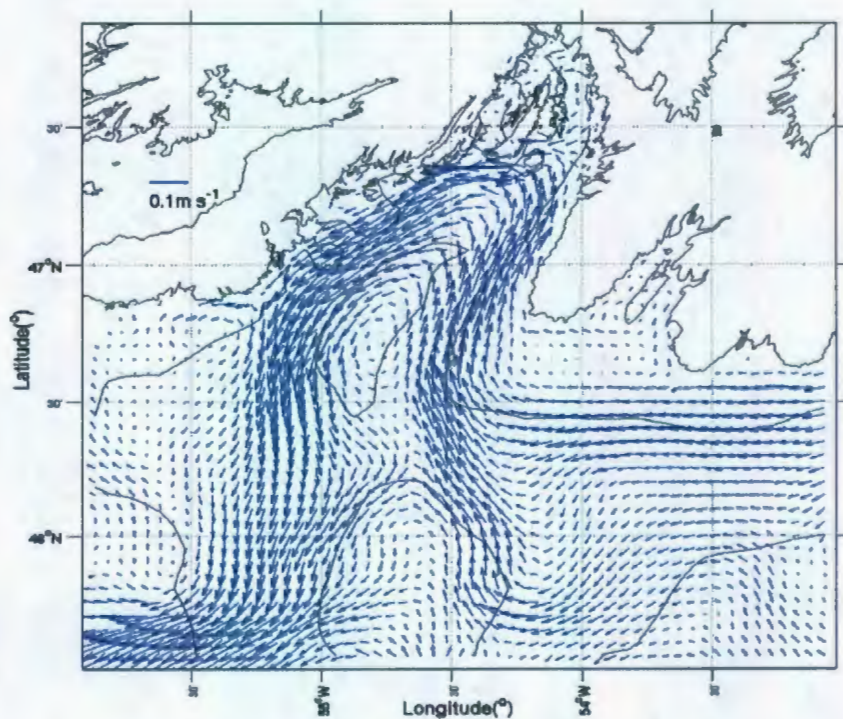


Figure (5-7): velocity transect along the 47 °N at three different time point (a):April-19-18:00 and (b) May-21-0:00 (c) June-15-0:00.

5.7 Mean Circulation and Transport

As shown in previous studies (Petrie and Anderson 1983; Greenberg and Petrie 1988; Han *et al*, 2008), the Labrador Current runs along the Newfoundland coast and shelf edge and splits into three branches at the north of Grand Bank, one of inshore weak branch of the Labrador current flows westward along Avalon Channel into the current model domain. To detect basic horizontal circulation over the current domain, model mean currents at 20 m are calculated from the mean of the whole model running period from year day 94.75 to day 182. As shown in Figure 5-8(a), currents at 20m below the surface indicate a dominant counter clockwise flow along the coastline. An inshore current from Avalon Channel flows around Cape Race, and separates into two branches, one flowing offshore through Haddock channel, the other continuing along coastline into the eastside mouth of Placentia Bay with the shoreline on its right (following the f/H contour line, where f is the Coriolis parameter and H is the water depth). This topographically steered current has a magnitude of 10 cm/s , reaches $47.5^\circ N$, turns around Red Island to the east side of Placentia Bay, and moves along the eastern coastline of the Bay to flow out of the bay mouth on the other side. One of this outer bay current flows toward the St.

Pierre Bank to join the offshore Labrador Current, while the other follows the coastline as expected for the propagation of Kelvin Waves (deYoung *et al.*, 1993). The near bottom circulation is not substantial overall, but a bottom flow can be seen along the east coast of the Bay, indicating the importance of the barotropic effect there (Figure 5-8 (b)).



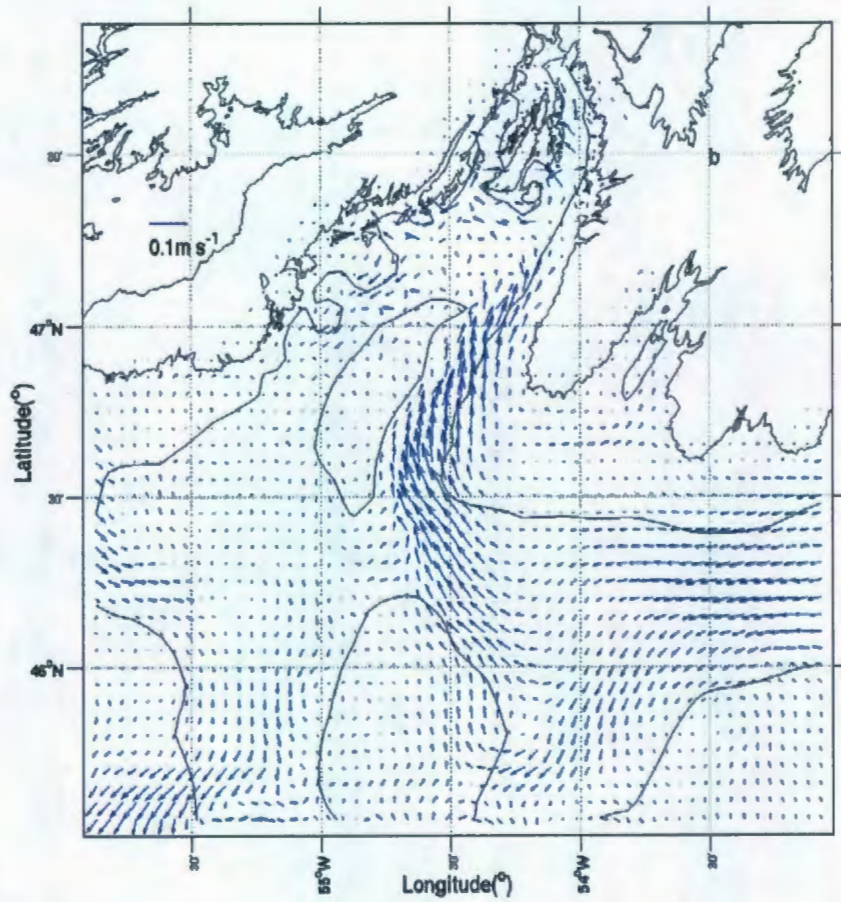


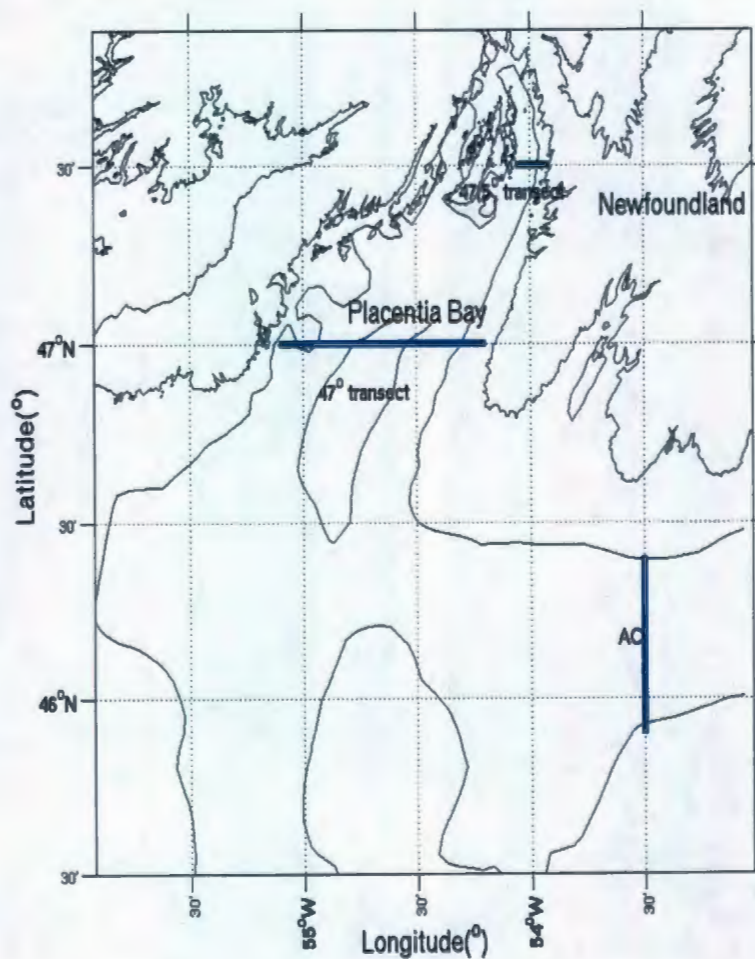
Figure (5-8): Model mean currents from year day 94.75 to 182 at the (a) 20m below the surface and (b) $\sigma = 0.995$ circulation.

5.8 Transport

In this section we investigate the fluxes of water through various Placentia Bay cross sections and demonstrate that the FVCOM conserves mass over long simulation intervals. Two sections are across $47^{\circ}N$ and Avalon Channel (Figure 5-9a). Positive transport is eastward or northward. The mean transport during the model period through Avalon channel is $0.33 S_v$ in the present study while the mean transport inshore 100 m isobath is $0.40 S_v$. The total transport through the Avalon channel was estimated to be $0.39 S_v$ on the basis of current meter data (Greenberg and Petrie, 1988). As shown in the Figure 5-9 (b), the Avalon Channel transport suggests a decreasing seasonal trend from spring to early summer time which is consistent with the previous seasonal transport study at near shore Flemish pass transect (Han et al. 2008). The synoptic timescale feature occurs over time because of shifting wind. Figure 5-9(c) shows the times series transport along $47^{\circ}N$ with a mean transport $0.0089 S_v$ to the north which means water flows into the inner bay through model time. The strong response with $0.12 S_v$ at days 95 is primarily from the open boundary which is also shown in the Avalon Channel transport plot (Figure 5-9 (b)). The mean transport difference between the Avalon Channel and the $47^{\circ}N$ is $0.32 S_v$ corresponded to the large water out flow through Avalon Channel into the

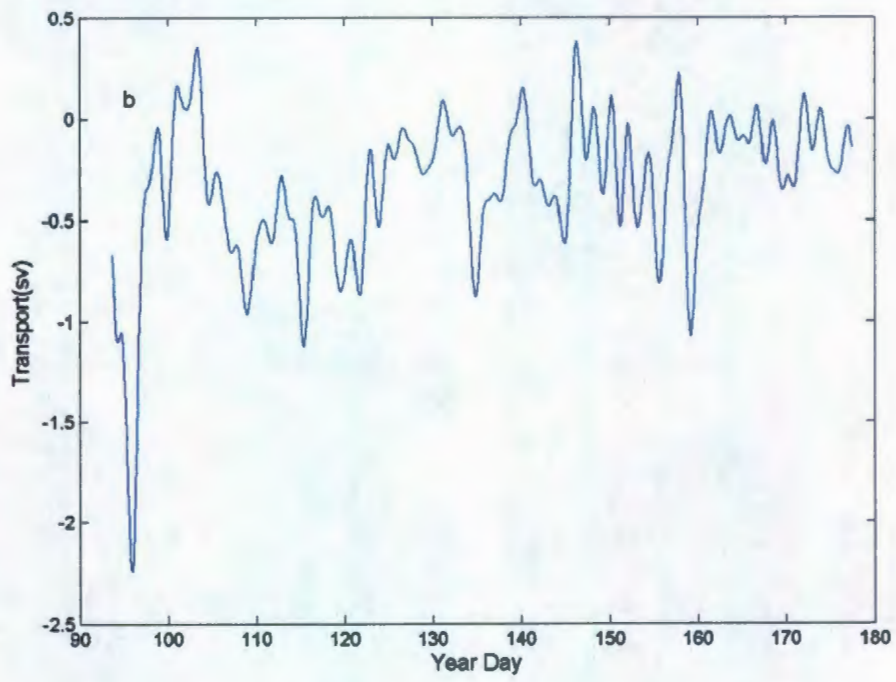
shelf edge. Highly variable transports between positive and negative from day 99 to day 107 may be caused by the wind (see wind plot Figure5-1(a)).

(a)

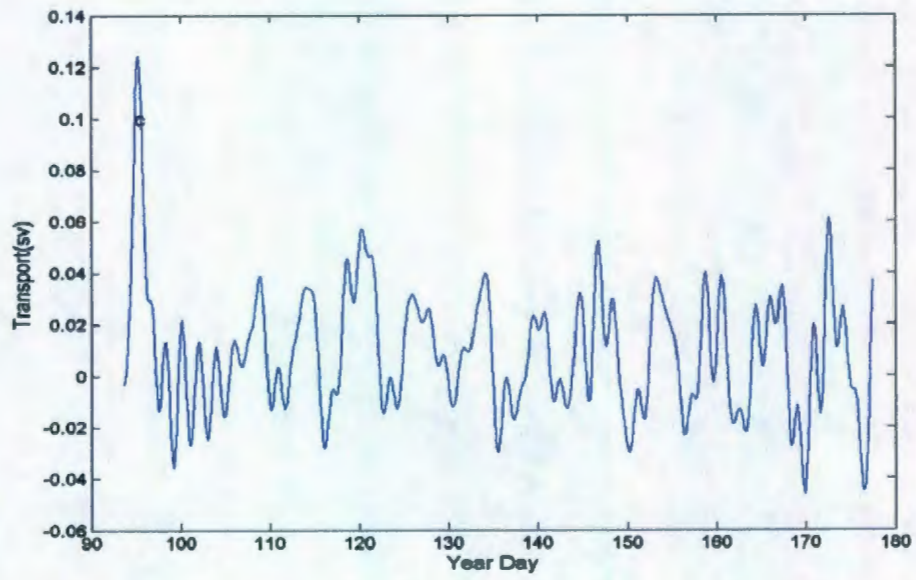


Figure(5-9): map showing the Placentia Bay. The isobaths displayed are 100 and 200m. Avalon channel(AC) (a) transect location Three transport times series plots for (b) Avalon Channel (between 100m contour) (c) transect at $47^{\circ}N$. Values are detided using the 36 cutoff frequency low filter.

(b)



(c)



(Continued)

6. Summary and future work

The FVCOM 3D model provided a good simulation of circulation and temperature. The model correctly reproduced the bay circulation generated by northeasterly winds during the spring time, as well as the upwelling process caused by the southwesterly winds during the early summer time. The simulated cyclonic bay circulation patterns agree well with the previous field measurement (Hart *et al.*, 1999). For the daily time scale features, our model can reproduce it, especially in M3 at 20m (Figure 5-6) except the currents around day 120 due to the underestimate of input flux from open boundary. The relatively poor correlation between observed and simulated along-bay currents on the western side of bay (Figure 5-6 and Table 5-5) was likely due to the underestimation of the baroclinic effect caused by the poor knowledge of initial salinity distribution, neglect of the freshwater input at the head of the inner bay, and over-smoothing of bathymetry as noted in chapter 5.

Semidiurnal tidal constituents from model results were well predicted compared with the two tidal elevation gauge data and five tidal current mooring stations. The dominant M_2 tidal currents were well reproduced and thus justified model abilities to simulate the tide. Tidal

elevation spread as the path of Kelvin wave to be consistent of the previous knowledge of tidal development on Newfoundland shelf (Han 2000).

The hydrographic distribution in Placentia Bay was examined and developed through spring time to early summer time. The seasonal temperature trend and stratification evolution are well represented by the model. With the RMS differences and γ^2 value showed in Table 5-1 to 5-4, our model temperature shows a good comparison with the observation. However, we still find the RMS difference is relatively large around 1.5 °C at 10 m. This temperature difference is due to the fact that model temperature is warmer than the observed value based on Figure 5-2 a,b,. This higher near surface temperature is probably because of the more shortwave input from the heat flux calculation (Curry and Webster, 1999) and insufficient turbulent. Furthermore, the temperature vertical transect also suggest the existence of the middle cold water layer.

For future work, fresh water discharge needs to be added to force the inner bay salinity horizontal development and water flux distribution. Higher resolution with 100 m grids or even higher is required to better present the topography change over the inner bay.

As we know, marine ecology plays an important role in the

development of cod or other marine lives in Placentia Bay. To better understand the ecology system in Placentia Bay, the model results will be applied to analysis the annual variability or even yearly trend of the ecology system in Placentia Bay such as the variability of the surface chlorophyll induced by currents and temperature. With enough knowledge of the ecology system in Placentia Bay, we can expect the spawning time of the cod in a particular year and some other cod events.

References

- Barth,T.J., and D.C.Jespersen, 1989, The design and application of upwind scheme on unstructured meshes.AIAA paper 1989-0366.
- Bradbury,I.R., Snelgrove,P.V.R., and Fraser,S., 2000, Transport and development of eggs and larvae of Atlantic cod,*Gadus morhua*, in relation to spawning time and location in coastal Newfoundland,Canadian journal of fisheries and aquatic sciences, 57, 1761-1772.
- Bradbury,T.R., B.J.Laurel., D.Robichaud, G.A.Rose, P.V.R.Snelgrove, R.S.Gregory,D.Cote, M.J.S.Windle, 2008, Discrete spatial dynamics in a marine broadcast spawner: Re-evaluating scales of connectivity and habitat associations in Atlantic cod (*Gadus morhua* L.) in coastal Newfoundland, Fisheries research, 91, 299-309.
- Burchard.H., 2001, Simulating the wave-enhanced layer under breaking surface waves with two-equation turbulence models, Journal of physical oceanography, 31, 3133-3145.
- Chapman,D.C, 1985. Numerical treatment of cross-shelf open boundaries in a barotropic coastal ocean model, Journal of physical oceanography, 15, 1060-1075.
- Chen,C, and H.Liu, 2003, An unstructured grid,finite-volume,three-dimensional, primitive equation ocean model: application to coastal and estuaries, Journal of atmospheric and oceanic technology, 20,159-186.
- Chen,C, R.C.Beardsley, P.J.S.Franks and J.V.Keuren, 2003b, Influences of the diurnally varying heat flux on stratification and residual circulation on Georges Bank, J.Geophys.Res.,108(C11),8008.
- Chen,C,G.Cowles and R.C.Beardsley, 2004b , An unstructured grid, finite-volume coastal ocean model : FVCOM User Manual. SMAST/UMASSD Technical Report-04-0601, pp183.
- Curry,J.A, Webster,P.J, 1999, Thermodynamics of atmospheres and oceans.Volume 65, Academic Press; 1st edition. 471 PP.
- deYoung,B., Otterson,T. and R.Greatbatch, 1993. The local and nonlocal response of conception bay to wind forcing, J.Phys.Ocean., 23, 2636-2649.
- deYoung,B., and Rose,G.A., 1993. On recruitment and the distribution of Atlantic cod(*Gadus morhua*) off Newfoundland. Can.J.Fish.Aquat.Sci,50, 2729-2714.
- Fairall,C.W., Bradley,E.F., Rogers,D.P., Edson,J.B., Young,G.S.,1996. Bulk parameterization of air-sea fluxes for COARE. 8th Conference on Air-Sea Interaction/Conference on the Global Ocean-Atmosphere-Land System (GOALS)

ATLANTA, GA, J1-J6.

Frank, K.T., and W.C. Leggett, 1982. Coastal water mass replacement: its effect on zooplankton dynamics and the predator-prey complex associated with larval capelin (*Mallotus villosus*). *Can. J. Fish. Aquat. Sci.*, 39, 215-223.

Fung, I.Y., Harrison, D.E., Lacis, A.A., 1984. On the variability of the net long-wave radiation at the ocean surface, *Rev. Geophys. Space Phys.*, 22(2), 177-193.

Galperin, B., L.H. Kantha, S. Hassid, and A. Rosati, 1988. A quasi-equilibrium turbulent energy model for geophysical flows, *J. Atmos. Sci.*, 45, 55-62.

Geshelin, Y., J. Sheng, and R.J. Greatbatch, 1999. Monthly mean climatologies of temperature and salinity in the western North Atlantic, *Can. Tech. Rep. Hydrogr. Ocean Sci.* 153, 62 pp., Ocean Sci. Div. of Fish. and Ocean Can., Dartmouth, N. S., Canada.

Greenberg, D.A., and B.D. Petrie, 1988. The mean barotropic circulation on the Newfoundland shelf and slope, *Journal of geophysical research*, 93, 15541-15550.

Han, G., 2000. Three-dimensional modeling of tidal currents and mixing quantities over the Newfoundland shelf, *Journal of geophysical research*, Vol 105, No, C5, 11407-11422.

Han, G., 2005. Wind-driven barotropic circulation off Newfoundland and Labrador, *Cont. shelf Res.*, 25, 2084-2106.

Han, G., Z. Lu., Z. Wang., J. Helbig., N. Chen., deYoung, B., 2008. Seasonal variability of the Labrador Current and shelf circulation off Newfoundland., *Journal of geophysical research*, 113, 1-23.

Hart, D.J., deYoung, Brad., J. Foley., 1999. Observations of currents, temperature and salinity in Placentia Bay, Newfoundland 1998-9.

Huang, H., Chen, C., G.W. Cowles, C.D. Winant, R.C. Beardsley, K.S. Hedstrom and D.B. Haidvogel. 2008. FVCOM validation experiment: comparisons with ROMS for three idealized barotropic test problems.

<http://fvcom.smast.umassd.edu/FVCOM/FVCOMpubs/index.html>.

Hubbard, M.E., 1999. Multidimensional slope limiters for MUSCL-type finite volume schemes on unstructured grid. *J. comput. Phys.*, 155, 54-74.

Kraus, E. B., 1972. *Atmosphere-Ocean Interaction*. Clarendon Press, 275pp.

Kobayashi, M.H., J.M.C. Pereira and J.C.F. Pereira, 1999. A conservative finite volume second order accurate projection method on hybrid unstructured grids. *J. Comput. Phys.*, 150, 40-75.

- Lawson,G.L., and G.A.Rose, 2000. Small-scale spatial and temporal patterns in spawning of Atlantic cod(*Gadus morhua*) in coastal Newfoundland waters. *Can.J.Fish.Aquat.Sci*,57, 1011-1024.
- Li,J, J.Scinocca, J.Lazare ,M.McFarlane, N.McFarlane, K.von Salzen, and L.Solheim. 2006. Ocean surface albedo and its impact on radiation balance in climate model.*Journal of Climate*.Volume 19,6314-6333.
- Madala,R.V., and S.A.Piacsek., 1977.A semi-implicit numerical model for baroclinic oceans,*J.Comput.Phys.*,23,167-178.
- Mellor,G.L, and T.Yamada, 1982. Development of a turbulence closure model for geophysical fluid problems. *Rev.Geophys.*, 20, 851-875.
- Mellor,G.L, T.Ezer, and L.Y.Oey, 1993. The pressure gradient conundrum of sigma coordinate ocean models, *Journal of atmospheric and oceanic technology*, 11,1126-1134.
- Mellor,G.L, and A.Blumberg, 2004. Wave breaking and ocean surface layer thermal response, *J.Phys.Oceanogr.*,34, 693-698.
- Monahan,E.G, and G.MacNiocaill, 1986, *Oceanic whitecaps and their role in air-sea exchange processes*. Springer-Verlag New York,LLC, 312PP.
- Paulson,C.A., and J.J.Simpson, 1977. Irradiance measurements in the upper ocean. *J.Phys. Oceanogr.*,7, 952-956,
- Pawlowicz,R., B.Beardsley, and S.Lentz., 2002. Classical tidal harmonic analysis including error estimates in MATLAB using T_TIDE. *Computers and Geosciences*. 28(2002),929-937.
- Pedlosky,J., 1974. Longshore currents, upwelling and bottom topography. *J.Phys. Oceanogr.*, 4,214-226
- Pepin,P., J.A.Helbig, R.Laprise, E.Colbourne, and T.H.Shears, 1995. Variations in the contribution of transport to changes in animal abundance: a study of the flux of fish larve in Conception Bay, Newfoundland. *Can.J.Fish.Aquat.Sci*, 52, 1475-1486.
- Petrie,B., and C.Anderson, 1983. Circulation on the Newfoundland continental shelf, *Atmos.Ocean*,21,207-226.
- Rose,G.A., deYoung,B., Kulka.,D.W., Goddard,S.V., and Fletcher,G.L., 2000. Distribution shifts and overfishing the northern cod(*Gadus morhua*): a view from the ocean. *Can.J.Fish.Aquat.Sci*, 57, 644-664.

Ruzzante,D.E., Wroblewski,J.S., Taggart,C.T., Smedbol,R.K., Cook,D., and Goddard,S.V., 2000. Bay-scale population structure in coastal Atlantic cod in Labrador and Newfoundland. *Can.J.Fish Biol.*, 56,431-447.

Schillinger,D.J., Simmons, P., and deYoung, B, 2000. Analysis of the mean circulation in Placentia Bay: spring and summer 1999, Physics and physical oceanography data report 2000-1.

Simpson,J.J., and T.D.Dickey, 1981a. The relationship between downward irradiance and upper ocean structure,*J.Phys.Oceanogr.*,11,309-323.

Simpson,J.J., and T.D.Dickey, 1981b. Alternative parameterizations of downward irradiance and their dynamical significance,*J.Phys.Oceanogr.*,11,876-882.

Smagorinsky,J., 1963. General circulation experiments with the primitive equations, 1, The basic experiment. *Monthly Weather Review*, 91:99-164.

Smedbol,R.K., D.S.Schneider, J.S.Wroblewski, and D.A.Methven, 1998. Outcome of an inshore spawning event by northern Atlantic cod(*Gadus morhua*) at a low stock level. *Can.J.Fish. Aquat.Sci.*55, 2283-2291.

Snelgrove,PVR, Bradbury,IR, deYoung,B and Fraser,S, 2008. Temporal variation in fish egg and larval production by pelagic and bottom spawners in a large Newfoundland coastal embayment, *Journal of fisheries and aquatic sciences*, vol 65 ,159-175.

Stacey,M.W., 1999. Simulation of the wind-forced near-surface circulation in Knight Inlet: a parameterization of the roughness length, *Journal of physical oceanography*, 29, 1363-1367.

Taggart,C.T., and W.C.Leggett, 1987. Short-term mortality in post emergent larval capelin *Mallotus villosus*,II, Importance of food and predator density, and density dependence.*Mar.Ecol.Prog.Ser.*41, 219-229.

Tang,C.L., Q.Gui, I.K.Peterson, 1996. Modeling the mean circulation of the Labrador sea and adjacent shelves, *J.Phys.Oceanogr.*,26,1989-2010.

Terray,E.A., M.A.Donelan, Y.C.Agrawal, W.M.Drnnan, K.K.Kahma, A.J.Williams, P.A.Hwang, and S.A.Kitaigorodski, 1996. Estimates of kinetic energy dissipation under breaking waves. *J.Phys.Oceanogr.*, 26, 792-807.

Terray,E.A., M.A.Donelan, Y.C.Agrawal, W.M.Drnnan, K.K.Kahma, A.J.Williams, P.A.Hwang, and S.A.Kitaigorodski, 1997. Reply. *J.Phys.Oceanogr.*, 27, 2308-2309.

Terray,E.A., W.M.Donelan, and M.A.Donelan, 2000. The vertical structure of shear and dissipation in the ocean surface layer. *Proc. Symp. On Air-Sea Interaction Sdney*,

Australia, University of New South Wales,239-245.

